Early diagenesis at and below Vera Rubin ridge, Gale crater, Mars

Stuart M R Turner, S. P Schwenzer, J. C Bridges, E. B Rampe, C. C Bedford, C. N Achilles, A. C Mcadam, N. Mangold, L. J Hicks, J. Parnell, et al.

Early Diagenesis at and below Vera Rubin ridge, Gale crater, Mars

S. M. R. Turner[1], S. P. Schwenzer[1], J. C. Bridges[2], E. B. Rampe[3], C. C. Bedford[3,4,5], C. N. Achilles[6], A. C. McAdam[6], N. Mangold[7], L. J. Hicks[2], J. Parnell[8], A. A. Fraeman[9], M. H. Reed[10]

[1]AstrobiologyOU, School of Environment, Earth and Ecosystem Sciences, The Open University, UK.

[2]Space Research Centre, School of Physics and Astronomy, University of Leicester, UK.

[3]NASA Johnson Space Center, USA.

[4]School of Physical Sciences, The Open University, UK.

[5]Lunar and Planetary Institute, Universities Space Research Association, USA.

[6]NASA Goddard Space Flight Center, USA.

[7]Laboratoire de Planétologie et Géodynamique, UMR6112 CNRS, Université de Nantes, Université Angers, France.

[8]School of Geosciences, University of Aberdeen, UK.

[9]Jet Propulsion Laboratory, California Institute of Technology, USA.

[10]Department of Earth Sciences, University of Oregon, USA.

Corresponding author: Stuart Turner (stuart.turner@open.ac.uk).

Abstract

Data returned by NASA's Mars Science Laboratory *Curiosity* rover showed evidence for abundant secondary materials, including Fe-oxides, phyllosilicates, and an amorphous component on and below Vera Rubin ridge in the Murray formation. We have used equilibrium thermochemical modeling to test the hypothesis that these altered sediments were deposited predominantly as detrital igneous grains and subsequently underwent diagenetic alteration. Chemical compositions of the altered components were calculated using data returned by the Chemistry and Mineralogy X-ray diffraction instrument and the Alpha Particle X-ray Spectrometer on board *Curiosity*. Reaction of these alteration compositions with a CO_2-poor and oxidizing dilute aqueous solution was modeled at 25 – 100 °C, with varying amounts of Fe^{3+}/Fe_{tot} of the host rock. The modeled alteration assemblages contained abundant phyllosilicates and Fe-oxides at >100 water to rock ratios, and were directly comparable to the abundances of hematite and clay minerals observed by *Curiosity* at 10,000 water to rock at 50 – 100 °C with pH ranging from 7.9 to 9.3. Our modeling results suggest that the hematite-clay mineral assemblage is primarily the result of enhanced groundwater flow compared to the Sheepbed mudstone in the Bradbury Group observed at Yellowknife Bay, and underwent further, localized alteration to produce the mineralogy observed by *Curiosity*.

1. Introduction

At Gale crater, a succession of lakebed sediments has been found in the Murray formation by the NASA Mars Science Laboratory (MSL) *Curiosity* rover (e.g., Grotzinger et al., 2015; Edgar et al., 2020, see Fraeman et al., 2020 for an overview of the entire geologic context). In this study we use thermochemical modeling to test the hypothesis that the sediments were deposited predominantly as detrital igneous grains followed by diagenetic alteration conditions where groundwater interacted with the sediments. This is in continuation of previous work at the first units encountered by *Curiosity* at Yellowknife Bay (Bridges et al., 2015b; Schwenzer et al., 2016). In doing so, we aim to constrain associated temperature, water to rock ratios, pH, and redox conditions of the early diagenetic alteration that resulted in the predominantly hematite-clay mineral assemblage observed in the Murray formation on and below Vera Rubin Ridge (VRR). We assume that vein formation as described in L'Haridon et al. (2020) and acidic alteration (Rampe et al., 2020b) belong to a later phase of alteration as well as Ca-sulfate formation, which has been shown to occur during a later step of fluid evolution (Schwenzer et al., 2016). The former is consistent with the sedimentological observations (Edgar et al., 2020) and observations by *Curiosity's* instruments (see, e.g., McAdam et al., 2020).

1.1 Overview of the Murray formation

The Murray formation was first encountered on sol 792 of the NASA MSL mission and constitutes the sedimentary units analyzed by the *Curiosity* rover from the foothills of Mount Sharp (Grotzinger et al., 2015). From orbit, the lower Murray formation has areas with orbital spectral signatures consistent with Fe/Mg clay, hydrated silica, iron oxides, and sulfate (Anderson and Bell, 2010; Milliken et al., 2010; Thomson et al., 2011; Fraeman et al., 2013; Fraeman et al., 2016). At the time of writing, the Murray formation is estimated to be ~300 m thick and has been subdivided into seven members that are separated by conformable contacts, as illustrated by Edgar et al. (2020). Briefly, the seven members are the Pahrump Hills, Hartman's Valley, Karasburg, Sutton Island, Blunts Point, Pettegrove Point and Jura, comprised of sand- silt and mudstones of lake bed and fluvial origin (Grotzinger et al., 2015; Bristow et al., 2018; Edgar et al., 2018; Fedo et al., 2018; Gwizd et al., 2018; Rivera-Hernandez et al., 2019; Stack et al., 2019; Edgar et al., 2020).

1.1.1 Stratigraphic members below Vera Rubin Ridge

Stratigraphic members below VRR of interest in this study were the Hartmann's Valley, Karasburg, Sutton Island, and Blunts Point members (Figure 1).

The Hartmann's Valley member (25 m thick) has grains ranging in size between silt to medium sand and with meter-scale, trough cross-bedding indicative of either fluvial or aeolian settings (Bristow et al., 2018; Fedo et al., 2018; Gwizd et al., 2018). The Oudam sample was drilled from this member, in fine-grained bedrock containing diagenetic Ca-sulfate mineral veins (Bristow et al., 2018).

The Karasburg member (37 m thick) in the Murray Buttes locality is characterized by a heterolithic mudstone/fine sandstone assemblage with abundant cm-scale concretions and a purple hue (Fedo et al., 2018). In this member, the samples Marimba and Quela were drilled from flat mudstone bedrock containing some small Ca-sulfate mineral veins and mm-scale concretions (Bristow et al., 2018; L'Haridon et al., 2018; Meslin et al., 2018).

The Sutton Island member (98 m thick), also contains a heterolithic mudstone/sandstone assemblage that is largely red in color and has an increased abundance of Ca-sulfate features (e.g., veins and lenticular crystals) and polygonal cracks interpreted to result from desiccation at the lake margins (Stein et al., 2018). The Sebina sample was drilled from flat, fine-grained bedrock that has abundant, cm-scale nodules and Ca-sulfate mineral veins.

The Blunts Point member (~100 m thick) is exposed immediately below VRR on the north-facing side and shares a conformable boundary with the ridge (Edgar et al., 2020; Fedo et al., 2018). The Blunts Point member is characterized by well laminated mudstone with cross-cutting curviplanar Ca-sulfate veins (Edgar et al., 2020). The Duluth drill sample was acquired near the base of VRR in a well laminated bedrock with diagenetic raised ridges and Ca-sulfate veins (Figure 1).

1.1.2 Stratigraphic members on Vera Rubin Ridge

VRR is a ~200 m wide ~6.5 km long northeast-southwest resistant geomorphological feature on the northern slopes of Mount Sharp (Figure 2). VRR is composed of the Pettegrove Point member that is overlain by the Jura member (Figure 1). They have a combined stratigraphic thickness of approximately 60 m and were investigated by *Curiosity* from sol 1809 to sol 2302, when *Curiosity* traversed off VRR. The lithology at VRR appears consistent with the Murray formation mudstones analyzed previously (Fedo et al., 2018; Heydari et al., 2018), with a grain size similarly dominated by mud and contains occasional intervals of fine to medium sandstone (Edgar et al., 2020; Rivera-Hernandez et al., 2019). APXS and ChemCam analyses in the Murray formation members below and on VRR indicate that it is compositionally continuous with the Murray formation, and that Fe concentrations are not elevated for VRR; this suggests the compositional trends from the rocks below and the rocks on VRR are largely the result of post-depositional processes, such as diagenesis (Thompson et al., 2020; Frydenvang et al., 2020).

Rocks within the Pettegrove Point member of the ridge are thin planar laminated, fine-grained mudstones. Rocks within the Jura member at the top of the VRR stratigraphic succession are also characterized by fine-grained and planar laminated facies, but with a greater degree of variability in color (red, purple, grey and tan) and meter-scale inclined strata (Edgar et al., 2018, 2020). Generally, rocks within the Pettegrove Point member have fewer diagenetic features such as nodules, mineral veins, fractures and erosion resistant features (L'Haridon et al., 2020), and are lower in Al_2O_3, SiO_2, and higher in FeO_T than the Jura member (Thompson et al., 2020). Both members are generally red/purple (Bennett et al., 2018) though grey bedrock patches up to ~10 m in diameter have also been detected along VRR but are more common in the Jura member (Frydenvang et al., 2020; L'Haridon et al., 2020). These grey patches are currently interpreted as resulting from diagenesis, possibly from the circulation of warm, oxidizing, fluids (e.g., Bibi et al., 2011; Peretyazhko et al., 2016, 2018; McAdam et al., 2020; Fraeman et al., 2020; Rampe et al., 2020b) or reducing groundwater (Frydenvang et al., 2020; Horgan et al., 2020; L'Haridon et al., 2020).

Three drill samples have been successfully delivered to CheMin from VRR. The Stoer drill hole sampled red bedrock in the Pettegrove Point member containing some very small scale (~1 mm in diameter) concretions and has the highest abundance of hematite in any sample so far analyzed by *Curiosity*. The drilled samples 'Highfield' and 'Rock Hall' were acquired in the Jura member in Grey and Red Jura respectively. The Grey Jura 'Highfield' sample was drilled at the Lake Orcadie locality, which is within a diagenetic grey patch with abundant Ca-sulfate veins,

Fe-rich nodules and dark, elongate diagenetic features. MAHLI images before and after drilling showed that Highfield had potentially sampled these features. The Highfield sample is also notable for the likely presence of 'grey hematite' i.e. relatively coarse hematite with crystallites >5 μm in diameter (Rampe et al., 2020b). On the basis of Catling and Moore's (2003) study of grey hematite, Rampe et al. (2020b) inferred a lower temperature limit of ~100 ˚C for the grey hematite-bearing assemblage. The Rock Hall Jura sample was acquired just south of the grey Lake Orcadie area in a red patch of bedrock with an unusual, shiny, nodular appearance.

1.1.3 Mineralogy of the Murray formation

CheMin analyzed drilled rock powders from the Murray samples Confidence Hills, Mojave2, Telegraph Peak, Buckskin, Oudam, Marimba, Quela, Sebina, and Duluth below VRR, and Stoer, Highfield, and Rock Hall on VRR itself (for details on the methodology see Rampe et al., 2020a). Of these drilled rock powders, the last eight (Oudam through Rock Hall) belong to the hematite-clay mineral group investigated in this paper. CheMin data analyses show the presence of both detrital igneous minerals and products of aqueous alteration in these eight drilled rock powders. Details on the mineralogy of these samples are reported by Bristow et al. (2018), Rampe et al. (2020a), Achilles et al. (2020), and Rampe et al. (2020b). All eight samples contain abundant primary magmatic minerals in the form of plagioclase feldspar (19 – 24 wt.% of the bulk sample) with unit-cell parameters consistent with an andesine composition and lesser amounts of pyroxene (1 – 9 wt.% of the bulk sample), alkali feldspar (<3 wt.% of the bulk sample) and quartz (<1 wt.% of the bulk sample). The low angular resolution of the CheMin instrument prevents a confident identification of the type(s) of pyroxene present (Rampe et al. 2020b).

Phyllosilicates are present in every sample but vary in structure and abundance through the stratigraphy. Ferripyrophyllite ($Fe_2Si_4O_{10}(OH)_2$), a member of the talc-pyrophyllite group, is the most likely phyllosilicate in Oudam (3 ± 1 wt.% of the bulk), based on position and breadth of the low intensity (001) basal peak (9.6 Å in CheMin data) and the H_2O evolution profile observed from the Oudam SAM EGA analysis (Bristow et al., 2018; Achilles et al., 2020). In Marimba, Quela, and Sebina the phyllosilicate basal spacings and the positions of the (02*l*) band suggest a mix of dioctahedral and trioctahedral smectite (e.g., Bristow et al., 2018). Smectite composes 28 ± 3 wt.% of the bulk of Marimba, and the (02*l*) peak position is consistent with a 1:2 dioctahedral:trioctahedral weight abundance ratio, with SAM EGA data consistent with Fe-montmorillonite and Mg-saponite (Bristow et al., 2018; Achilles et al., 2020). Dioctahedral:trioctahedral ratios for the 16 ± 2 wt.% smectite in Quela and the 19 ± 2 wt.% smectite in Sebina are 1:1 and 5:3, respectively, based on CheMin data (Bristow et al., 2018; Achilles et al., 2020). Data from Duluth indicate the presence of exclusively dioctahedral smectite. Analysis of CheMin data for Duluth indicates 15 ± 7 wt.% bulk Fe^{3+} clay, with both CheMin (Rampe et al., 2020b) and SAM EGA data (McAdam et al., 2020) consistent with the presence of nontronite. The basal spacings in the patterns from Stoer, Highfield, and Rock Hall are at 9.6 Å instead of the 10 Å position attributed to collapsed smectite in previous samples (Bristow et al., 2018), indicating the presence of a collapsed smectite with a small interlayer cation or the trioctahedral phyllosilicate ferripyrophyllite (Bristow et al., 2018; Rampe et al., 2020b). Phyllosilicate abundances for Stoer, Highfield and Rock Hall were reported to be 10 ± 5, 5 ± 2 and 13 ± 6 wt.% bulk, respectively (Rampe et al., 2020b). Overall, the abundance and nature of the clay minerals in conjunction with primary magmatic minerals, allows for testing the

hypothesis that all or a significant proportion of the clay minerals were formed in situ during post-depositional diagenesis.

Each drill sample contains abundant Fe-oxides and/or Fe-oxyhydroxides (Achilles et al., 2020; Rampe et al., 2020b). Hematite (α-Fe_2O_3) is present in every sample in abundances of ~3 wt.% of the bulk sample for Rock Hall up to ~16 wt.% of the bulk sample for Stoer. The colors of the drill tailings in Oudam and Highfield suggest grey or specular hematite is present in these samples. Akaganeite (α-$Fe^{3+}O(OH,Cl)$) is more abundant than hematite in Rock Hall, and constitutes 6 wt.% of the bulk sample. A trace amount of akaganeite is present in Stoer. Magnetite is present in Duluth, Stoer, Highfield, and Rock Hall near the detection limit of CheMin (Rampe et al., 2020b).

Ca-sulfate minerals are prevalent in every sample, but vary in type and abundance between samples. Most samples have all three varieties of Ca-sulfate (anhydrite – $CaSO_4$, bassanite – $CaSO_4 \cdot 0.5H_2O$, and gypsum – $CaSO_4 \cdot 2H_2O$), with the exception of Rock Hall. Rock Hall has the greatest abundance of Ca-sulfate of these samples, in which ~11 wt.% of the bulk sample is comprised of anhydrite. Duluth has the lowest abundance of Ca-sulfate of these samples, with ~1.5 wt.% anhydrite, ~3.5 wt.% bassanite, and gypsum is at the CheMin detection limit. Jarosite ($KFe_3(SO_4)_2(OH)_6$) is present in abundances up to a few wt.% in Marimba, Quela, Sebina, Stoer, and Rock Hall (Achilles et al., 2020; Rampe et al., 2020b).

All samples contain abundant X-ray amorphous materials, and FULLPAT analyses indicate that opal-CT comprises a portion of the X-ray amorphous materials in the Oudam and Highfield samples. Based on mass balance calculations using CheMin mineral abundances, crystal chemistry using CheMin mineral abundances, crystal chemistry, and bulk APXS measurements, the composition of the X-ray amorphous component is variably enriched in Si, Fe, and S in these samples (Achilles et al., 2020; Rampe et al., 2020b).

Several hypotheses exist for the variations in mudstone mineralogy such as variations in redox within the lake during the deposition of the Murray sediments (Hurowitz et al., 2017), a combined effect of source composition, mineral transportation and alteration (Bedford et al., 2019), diagenetic alteration at cold to low-T hydrothermal temperatures (Achilles et al., 2020; Frydenvang et al., 2020; McAdam et al., 2020*;* Thompson et al., 2020; Fraeman et al., 2013, 2016; Rampe et al. 2017), or aqueous alteration of deposited sediments by a short-lived, acidic fluid during late diagenesis (Rampe et al., 2017).

2. Methods

Thermochemical modeling is a useful tool to disentangle reaction pathways in environments where a fluid has interacted with a rock and changed its initial mineralogy, especially for martian environments where observations are limited compared to more accessible environments on Earth. On Mars, a wide range of reaction pathway problems have been studied successfully using a variety of thermochemical tools. On the basis of Martian meteorite and orbital data, problems such as carbonate and acidic reactions, silicate deposition, and organic molecule reactions have been studied and tested successfully against experimental or observational results (Griffith & Shock, 1995, 1997; Hausrath et al., 2018; McAdam et al., 2008; Tosca et al., 2004, 2008; Varnes et al., 2003; Zolotov and Mironenko, 2007, 2016; Zolotov and Shock, 1999, 2005). CHIM-XPT and its predecessor CHILLER have been used to study a wide range of Martian P-T regimes, mainly for clay forming environments (Bridges and Schwenzer,

2012; Filiberto and Schwenzer, 2013; Schwenzer and Kring, 2009, 2013; Schwenzer et al., 2012), and also successfully tested against observational ground truth in meteorites (Bridges and Schwenzer, 2012; Melwani-Daswani et al., 2016) and in situ on Mars (Bridges et al., 2015b; Schwenzer et al., 2016; Schieber et al., 2017). It is on this basis that CHIM-XPT was used to develop and test the models presented here.

Thermochemical modeling does, however, have limitations where extrapolation of pressure-temperature thermochemical data increases uncertainty, or kinetics changes the outcome of a reaction pathway compared to prediction made solely on Gibbs free energy calculations. For details on this background, we refer readers to a wide range of literature (e.g, Ganguly, 2008; Holland and Powell, 1998; Kühn, 2004; Reed, 1997; Rimstidt, 2014), which will provide the theoretical backing of the technique and further insights into problem solving and decision making to limit the impact of the tool's limitations. It is noted that clay minerals pose a problem in modeling iron-bearing environments on Mars (Catalano, 2013; Chevrier et al., 2007). Therefore, in this paper, care was taken to use all information available to constrain the modeling parameters when evaluating the results. It is important to note that in a sedimentary environment, or any dynamic geologic environment, the models describe reaction pathways of local equilibrium and not an overall equilibrium of the entire geologic unit (Kühn, 2004; especially chapter 3 and the critical discussion on p. 79f. for a more detailed discussion of the problem). Thus, such models enable the assessment of a reaction pathway for a given overall chemistry to reach the resulting alteration assemblage.

2.1 Thermochemical code and database

CHIM-XPT (Reed et al., 2010) is a program for computing multicomponent heterogeneous chemical equilibria in aqueous-mineral-gas systems and was chosen because of its heritage in modeling basaltic and ultramafic systems (e.g., Reed, 1983; Palandri and Reed, 2004), and modeling alteration on Mars (Schwenzer and Kring, 2009; Bridges and Schwenzer, 2012; Schwenzer et al., 2012; Filiberto and Schwenzer, 2013; Bridges et al., 2015b; Schwenzer et al., 2016; Melwani-Daswani et al., 2016; Schieber et al., 2017). Every calculation step calculates equilibrium between the fluid and the dissolved rock, meaning that each step can be treated and interpreted independently to the direction from which it was reached, and each step determines the properties of the minimum Gibbs free energy of the system. Step size may vary depending on task requirements. A weight ratio of the total number of fluid grams relative to the total number of grams of reactant rock is used, so model calculations are independent of the size of the system, but the calculations are usually based on 1 kg (55.5 mol) of water. Precipitates are not fractionated from the system unless stated otherwise. In CHIM-XPT, the water to rock ratio (W/R) is the ratio of incoming fluid to reacted host rock. Inputs required for the execution of CHIM-XPT in this study were the starting fluid composition, reactant rock chemical composition, system temperature and pressure. We did not include a gas phase at the start of the calculations and did not replenish any CO_2 or other components typically found in the Martian atmosphere. Thus, our system was closed to the atmosphere, as could be expected from a subsurface fluid. We note, that gas phases were allowed to form, should they have become stable, but none were observed at the conditions that led to clay and hematite formation.

The SOLTHERM thermodynamic database used with CHIM-XPT in this study contains the following sheet silicates: talc (Mg, Fe, Mg-Al endmembers); pyrophyllite; chlorites (clinochlore, daphnite, Mn-chlorite, Al-free chlorite); kaolinite; illite; montmorillonite (Ca, K,

Mg, Na endmembers); beidellite (Ca, H, K, Mg, Na endmembers); nontronite (Ca-, H-, K-, Mg-, Na-nontronite); serpentine (antigorite, chrysotile, greenalite); sepiolite. The only member of the kaolinite group the database contains is kaolinite. There is no saponite, vermiculite, or hectorite in the database. Results are plotted in mineral abundance (wt.%) vs W/R, with chlorite endmembers (Fe^{2+} clay mineral) and nontronite endmembers (Fe^{3+} clay mineral) combined. Given the thermodynamic database is limited with regards to the full range of possible phyllosilicates, in this study the modeled phyllosilicate assemblages are summed to calculate an average clay mineral with average composition that is then taken as a chemical analogue to the clay minerals observed in Gale crater. This is consistent with previous approaches by Bridges et al. (2015b) and Schwenzer et al. (2016).

Critical evaluation of the results and comparison to terrestrial mineralogy are required to further evaluate the modeling results. Especially at lower temperature, extrapolation of the thermodynamic data from higher temperature might occur, which can lead to the occurrence of mineral phases not known to form at the given pressure-temperature range. This problem is dealt with through careful evaluation of every phase forming and exclusion of those known to not form in the given pressure-temperature range, owing to kinetic constraints at low temperature (Melwani-Daswani et al., 2016, supporting material). The temperature transition between the Fe-oxides, goethite and hematite, was taken into consideration for the modeling. As documented by Cornell and Schwertmann (2006; *and references therein*) fine grained goethite is stable ≤ 25 °C, relative to coarse grained hematite. However, in laboratory environments where ferrihydrite was stored as aqueous suspensions at 24 °C and pH between 2.5 and 12, both hematite and goethite form, with maximum hematite forming between pH 7 and 8 and maximum goethite forming at pH 4 and pH 12 (Schwertmann and Murad, 1983). It is noted that the formation of other Fe-oxides such as ferrihydrite, goethite and akaganeite may have occurred first in the sediments of Gale crater and later transformed to hematite via mechanisms documented by Cornell and Schwertmann (2006; *and references therein*). However, while those precursors could have been a factor in some of the rocks we are studying, such as those that had high amounts of Fe in their amorphous components, it is difficult to definitively identify poorly ordered/amorphous Fe phases such as ferrihydrite with *Curiosity's* payload, and at the time of writing there is no direct evidence for ferrihydrite. For the purposes of this modeling study we assume direct precipitation of goethite or hematite from the modeled porewater-rock interactions, and not from the alteration of ferrihydrite. Magnetite was allowed to form but did not under the conditions modeled here at the W/R assumed relevant.

A list of the minerals excluded in each model can be found in the supplementary material (Table S3). It should be noted that the model calculations show finer details than any of the sources of information from Mars: detection limit for CheMin on *Curiosity* is ~1 wt.% (Blake et al., 2012) and the pixel footprint of CRISM is nominally 18 m, (Murchie et al., 2007) limiting the detection of trace phases in both instances. Therefore, small contributions (<5 wt.%) of a modeled alteration assemblage may not be directly comparable to the observed martian mineralogy. Minerals modeled to form that have not been observed in the Murray formation, either in-situ with *Curiosity* or remotely with CRISM, were allowed to form due to a lack of justification for their removal.

2.2 Modeled water-rock ratio

CHIM-XPT thermochemically calculated mineral assemblages are illustrated in this manuscript as plots of mineral abundance (weight %) vs W/R ratio. W/R ratio is a progress variable where limited reactant rock dissolution occurs at high W/R with a relative increase in reactant rock dissolution at low W/R. The mass of alteration minerals precipitated ranges from 0.01 g at 100,000 W/R to 1000 g at 1 W/R. CHIM-XPT assumes complete dissolution of the defined reactant rock components in relevant W/R proportions per interaction step. While in real-world systems only partial host rock dissolution occurs (making the W/R values reported here comparably higher), modeling complete host rock dissolution enables a systematic investigation of modeled alteration minerals and associated fluids as a function of the W/R process variable. High W/R (>5,000) is representative of a system where only a small amount of the rock is dissolved in a large mass of fluid (i.e., where only a limited surface area interacts with the fluid and/or timescales are short).This can represent freshwater inflow environments such as in rock fractures or rock surfaces exposed to regular precipitation. Lower W/R ranges are more representative of little to no fresh-fluid inflow and stagnant fluids reacting with large rock surfaces. Comparison to experiments and geologic analogs show that W/R of around 1000 is generally comparable to water-rich diagenetic or small fracture settings, whereas lower W/R are comparable to low-water diagenetic and eventually metamorphic conditions. For an in-depth discussion how model and experimental water to rock ratios compare, see Olsson-Francis et al. (2017). CHIM-XPT calculates the equilibrium reaction of the fluid with the precipitating phases at an overall chemistry of the system.

3. Hypothesis and model set-up

The purpose of this study is to constrain the formation conditions (W/R, temperature, redox, pH) under which the hematite-clay mineral assemblage observed on and below VRR precipitated. More specifically, we test the hypothesis that the formation of clays and hematite in the Murray formation on and below VRR stands in a continuation of previous studies that assumed groundwater-type alteration. For Yellowknife Bay, the lowest point in the stratigraphy encountered by *Curiosity* early in the mission, studies showed that groundwater-type, circumneutral fluids could explain the clay mineral formation with sulfate formation happening during a second fluid evolution step (Bridges et al., 2015b; Schwenzer et al., 2016). Hausrath et al. (2018) came to a similar conclusion for Stimson formation alteration, where early olivine-dominant dissolution in circumneutral fluids and no redox-change is required to explain the observations. In this study, however, we focus on the alteration of a 'magmatic' host rock chemistry, as could be deposited by the fluvial-lacustrine conditions described for Gale crater, in a circumneutral groundwater.

There is a wide range of fluid-related observations and phenomena pre-VRR, such as overall lake water changes (Hurowitz et al., 2017), nodules (Nachon et al., 2014) and silica-rich haloes (Frydenvang et al., 2017), some of which are also observed on VRR. Other studies of VRR alteration (Fraeman et al., 2020; L'Haridon et al., 2020; McAdam et al., 2020; Rampe et al., 2020b; Yen et al., 2020) assume a multi-stage fluid evolution or a diversity of fluids to explain their observations, which gives further support to testing the hypothesis in this paper: that the first step of alteration was one of in situ diagenesis in a dilute, circumneutral fluid. This study is in context of the late-stage phases (Ca-sulfate, jarosite, akaganeite) forming when fluid concentrations had evolved to higher sulfate concentration, or more generally higher salinity, and

locally to acidic conditions (Achilles et al., 2020; L'Haridon et al., 2020; McAdam et al., 2020; Rampe et al., 2020b; Yen et al., 2020). This is further supported by SAM investigations of jarosite-bearing sediments showed a bimodal age distribution with a much younger potential formation age for the jarosite-bearing alteration (Martin et al., 2017). Therefore, modeling the reaction pathways of the late-stage Ca-sulfate, jarosite, and akaganeite is not a goal of this study.

3.1 The Starting Fluid

Gale Portage Water (GPW) (Bridges et al., 2015a, 2015b; Schwenzer et al., 2016; Turner et al., 2019) was used as the fluid in this study, making results presented here for the Murray formation directly comparable to the studies for Yellowknife Bay. This fluid was derived from equilibrium mediation between a fluid used previously in Mars fluid-rock interaction modeling (Schwenzer and Kring, 2009) and the basaltic Portage Soil composition sampled from the Rocknest aeolian bedform in Gale crater (Bish et al., 2013). This assumed that Rocknest can be regarded as an average crustal composition in Gale crater, and GPW is a fluid of groundwater-type concentration directly derived from local bedrock. Because of the dilute nature of this fluid, the chemistry of the rock reactants becomes the dominating factor in the water-rock reaction modeling. Thus, providing additional confidence that reaction pathways described here are directly applicable to *Curiosity's* observations in the Murray Formation. The exact W/R at which the rock composition dominates the reaction is dependent on the solubility of the element considered and its concentration in the rock. Influence of the fluid is highest for elements not contained in the rock, which mostly concerns volatiles such as CO_2. However, CO_2 concentration is low (1.68×10^{-4} mole/L) and does not typically lead to the formation of carbonates beyond trace level. A detailed summary of how this fluid was derived is given in Bridges et al (2015b), and the fluid composition in Table 3 of Bridges et al. (2015b). Chlorine concentrations are about an order of magnitude higher, at 5.76×10^{-3} mole/L, but chlorine is not observed to participate in mineral formation. It is an important carrier of ionic strength at the very highest W/R, but at the W/R considered important here, does not cause any change of the system. It also is a potential complexing anion to increase Fe-solubility (e.g., Cornell and Schwertmann, 2006), but Cl concentrations are too low to significantly increase Fe-concentration in the fluid (Bridges et al., 2015b). Our Fe-concentrations are generally in family with other similar models (e.g., Marion et al., 2003). Cl-concentrations only show notable influence on apatite formation, which forms as Cl-apatite instead of hydroxyl-apatite, if Cl-concentrations are significant, but forms F-apatite once fluorine is present (Filiberto and Schwenzer, 2013). We note that – due to the lack of quantitative fluorine data – we have not incorporated fluorine into the system. The solution is initially oxidizing with all S species as SO_4^{2-}, and the redox in the fluid is controlled by the SO_4^{2-} /HS^- pair. The redox of the system throughout each model is dependent on the Fe^{2+}/Fe^{3+} ratio of the total Fe in the reactant rock composition. The fluid composition is represented in each calculated step by a set of 112 different ionic species. Unless stated otherwise, fluid pH was modeled as a free parameter.

3.2 Host Rock Composition

The drill samples studied have a mixture of 'primary magmatic' phases, such as pyroxene and plagioclase (Achilles et al., 2020; Rampe et al., 2020b), and alteration phases such as phyllosilicates and hematite (Rampe et al., 2020b; McAdam et al., 2020). Olivine is absent in the samples, which is in agreement with many literature resources that have shown it to be the first mineral to dissolve (e.g., Gudbrandson et al., 2011; Hausrath et al., 2018). To model the first

diagenetic phase that occurred in the Murray formation, the chemistry of the observed alteration must be considered. In this study, chemical alteration compositions were calculated and used as the reactant host rock composition in the thermochemical modeling.

Calculating the chemical alteration compositions was undertaken by combining measurements taken by APXS and CheMin instruments on-board the *Curiosity* rover for drilled samples obtained in the Murray formation: Oudam, Marimba, Quela, Sebina, Duluth, Stoer, Highfield and Rock Hall (summarized in section 1.1). Using crystal chemistries derived for the magmatic minerals (Table S1) (Morrison et al., 2018; Achilles et al., 2020; Rampe et al., 2020b) and their abundances determined using CheMin data (Bristow et al., 2018; Rampe et al., 2020a), the associated compositional oxide wt.% contributions were subtracted from the bulk APXS measurements. Ca-sulfates observed by CheMin (Achilles et al., 2020; Rampe et al., 2020b) were also removed as these have been shown to have formed during late diagenesis (Nachon et al., 2014), during a possible two-step process (Schwenzer et al., 2016). This approach includes contributions from the amorphous component that, at the time of writing, is not well understood and is hypothesized to contain primary basaltic glass, nanophase Fe-oxides, amorphous sulfates, and sulfides (Bish et al., 2013; Smith et al., 2019; Rapin et al., 2019; Rampe et al., 2020a; Achilles et al., 2020; Wong et al., 2020).

Given the young, Amazonian age inferred from K-Ar investigations of the jarosite in the Mojave drill sample (Martin et al., 2017), it is also assumed that the observed akaganeite and jarosite formed during late-stage acidic alteration after the formation of hematite and clay minerals (e.g. Achilles et al., 2020; Rampe et al., 2020b). Thus, the formation of akaganeite and jarosite is not within the scope of this study. However, their chemical composition is included in the calculated alteration composition as their formation is likely the result of localized alteration where elements were remobilized from the products of the first step of diagenesis that is being modeled here.

3.3 Pressure-Temperature space

The temperatures selected for modeling were 25 °C, 50 °C, 75 °C and 100 °C, as this broad range can be consistent with the alteration mineralogy observed in Gale crater (Bristow et al., 2018; Rampe et al., 2020a). The pressure was selected to prevent boiling for each temperature. Results were then evaluated with respect to temperature and used as a guide for thermochemical modeling where reactant rock was the calculated chemical alteration compositions for drill samples collected in the Murray formation below VRR and the overall Murray formation.

3.4 Redox considerations

No direct measurements of overall redox conditions in the rock were possible (e.g., because of the presence of the amorphous phase; Achilles et al., 2020; Rampe et al., 2020b). Thus, different Fe^{2+}/Fe^{3+} ratios of the total Fe in the host rock were modeled. Resultant mineral assemblages were then compared to alteration mineral assemblages observed by *Curiosity* to evaluate the accuracy of the model. Models were run at Fe^{3+}/Fe_{tot} of the host rock chemistry at 10% and 50% to explore the varying effect on the resultant alteration mineral assemblage. SO_3 was recalculated as FeS and the equivalent amount of Fe was subtracted from FeO. Cl was recalculated as NaCl and the equivalent amount of Na was subtracted from Na_2O.

4. Model results

4.1 Calculation of the host rock composition

The result of the magmatic mineral subtraction process (section 3.2) shows a similar chemical alteration composition throughout the Murray formation below VRR (Figure 3). SiO_2 varies between 45 and 49 wt.% (Figure 3), FeO_T has a larger variation, between 23 and 29 wt.%, and a positive correlation with SiO_2. MgO varies between 5 and 7 wt.%, Al_2O_3 between 5 and 7 wt.%. Alkali oxides (Na_2O and K_2O) are below 2 wt.% in all calculated alteration compositions below VRR. The three samples acquired on VRR display a larger variability in SiO_2, varying from 35 to 54 wt.%. FeO_T has a similar variation to below VRR, varying between 23 and 29 wt.%. MgO is also similar in range on VRR compared to below, 3 to 6 wt.%, while Al_2O_3 is lower on VRR, ranging from 3 to 6 wt.%. Alkali oxides (Na_2O and K_2O) are below 2 wt.% in all calculated chemical alteration compositions on VRR.

For the VRR samples, there are some noteworthy observations for the chemical alteration compositions (Figure 3): The Rock Hall and Highfield drill holes sampled red and grey Jura, respectively, with the FeO_T in our calculation being about 5% higher in Rock Hall than in Highfield. The red Jura target, Rock Hall, is very similar in FeO_T to the red Pettegrove Point Stoer target. Generally, alteration assemblages high in SiO_2 appear low in FeO_T and vice versa, while Al_2O_3 is lowest when FeO_T is highest. When averaged over the entirety of the drilled samples, chemical alteration compositions below and on VRR are remarkably similar (Figure 4), pointing towards local element mobility. This confirms our assumption of a dilute incoming fluid, but also points towards the absence of a large-scale fluid movement in late-stage diagenesis after the formation of the hematite-clay dominant mineral assemblage.

The alteration content of the different samples was also assessed, with the ratio of alteration to primary mineral content detailed in Table 1. These ratios indicate that, if Ca-sulfates are excluded, samples below VRR contain a greater fraction of identified alteration products compared to VRR, with Duluth containing the least amount of alteration. This is consistent with Mangold et al. (2019a; 2019b) who showed a decrease in the Chemical Index of Alteration above the Sutton Island member. We have thus decided to model the average alteration composition of VRR and compare those models to models which use an overall average alteration composition and an average alteration composition for below VRR (excluding Duluth as this had further diagenetic features). A comparison of the mean alteration chemical compositions for the pre-VRR Murray formation (Oudam to Sebina) and for VRR Murray (Stoer to Rock Hall) shows that they are similar (Figure 4, see also Table S4) with the standard deviation of these mean compositions overlapping.

4.2 Alteration mineralogy in a groundwater-dominated setting

As described above, we assume that the sediments in the Murray formation on and below VRR are altered in situ from 'magmatic' detrital precursors, and our model with the calculated chemical alteration composition described above then allows us to compare a predicted mineral assemblage with what has been observed by *Curiosity* in the Murray formation. The reasoning for this is that what currently remains as unaltered pyroxene will not have taken part in the reactions, and what is now the alteration assemblage was once a 'magmatic' mineral, e.g. olivine, pyroxene, plagioclase, and has been reacted into the minerals we find now. Therefore, we modeled four temperature steps for the average VRR Murray alteration composition. The

resulting mineral assemblages for all three can be divided into three W/R sections. At very high W/R (above W/R of 10,000), models between 50 and 100 °C show a hematite-clay mineral assemblage whereby the dominant clay is chlorite (Figures 5 and 6). At 25 °C, goethite forms instead of hematite (Figures 5A and 6A). Between W/R of 10,000 and down to W/R of 100 or below, nontronite dominates, and below W/R of about 100 a talc-chlorite assemblage forms. This generalized pattern applies for different redox settings as well as for the VRR-only and 'all Murray' compositions (Figures 5, 6 and 7).

Assessing the influence on temperature in the system that has 10% of the FeO_T as Fe^{3+} (Figure 5A-D) shows that the W/R range in which nontronite forms becomes smaller and the amount of nontronite forming decreases as the temperature increases from 25 °C to 100 °C. Instead of nontronite, a hematite–chlorite assemblage forms at high W/R. Note also the increased presence of a SiO_2-phase with increasing temperature. At low W/R changes are more subtle, leading to the formation of a few wt.% of epidote at the highest temperature. This "metamorphic" assemblage is not found at Gale crater, for which reason we focus the discussion in the next section on the high and intermediate W/R sections.

In the case of the more oxidizing system (50% of the FeO_T as Fe^{3+}; Figure 6A-D), changes are subtle. Thermochemical models run at 25 °C show goethite abundances vary from 7.5 wt.%, 2.0 wt.% and 0.0 wt.% for models with 10% Fe^{3+}/Fe_{tot} to 9.6 wt.%, 1.6 wt.% and 5.2 wt.% for models with 50% Fe^{3+}/Fe_{tot}, at 10,000 W/R, 1,000 W/R and 100 W/R, respectively. At and above 50 °C, hematite is more thermodynamically stable than goethite and forms instead. As expected, hematite content increases with increasing Fe^{3+} availability, meanwhile Fe-sulfide decreases (Tables S5 and S6).

The nontronite field expands towards intermediate and lower W/R, and so does the SiO_2-phase, forming around W/R of 1,000 – 10,000 (Figures 5 and 6, Table S7). We note, though, that the overall pattern of a hematite-clay mineral assemblage at high W/R and nontronite at intermediate W/R remains stable (Table 2). However, at high W/R the dominant clays are chlorites, the onset of which occurs at lower W/R with increasing temperature (Figures 5 and 6). Modeling the different Murray averages (Table S4) at 50 °C and at 10% and 50% FeO_T as Fe^{3+} returns almost indistinguishable results (Figure 7), which demonstrates that the hematite-clay mineral assemblage is the dominant assemblage at high water to rock ratios over a wide range of environmental conditions.

4.3 Summary of the Modeled Alteration Mineral Assemblages

Thermochemical modeling undertaken for this study has focused on producing the hematite-clay mineral alteration assemblage observed in the Murray formation, with emphasis on sedimentary rocks on and below VRR. Chemical compositions of the alteration mineral assemblages observed by *Curiosity* were calculated and used as the reactant rock chemical compositions for thermochemical modeling. Modeled alteration mineral assemblages have been produced for a variety of W/R, temperatures and varying Fe^{3+}/Fe_{tot} content (Figures 5 and 6).

For the models in this study, at and above 50 °C hematite forms likely a result of it being more thermodynamically stable than goethite (Cornell and Schwertmann, 2006 *and references therein*) and makes these models directly comparable to observations by *Curiosity*. Table S5 gives details of the modeled hematite abundances showing an increase in hematite abundance with temperature at 10,000 and 1,000 W/R, with an additional increase associated with Fe^{3+}

availability. Magnetite was allowed to form in the models (Figures 5 and 6) but did not form at the W/R assumed relevant. Table S6 demonstrates that Fe-sulfide abundance increases with temperature at 10,000 W/R with minor wt.% variation at 1,000 W/R and 100 W/R. Fe-sulfide abundances decrease at all W/R with increased Fe^{3+} availability.

The dominant clay minerals, when formed in our thermochemical models belong to the smectite group (nontronite), though in some cases significant chlorites form. Clay mineral abundance varies significantly with temperature. In summary, the overall clay abundance decreases with temperature regardless of Fe^{3+} availability (Table S8); however, there is an increase in clay abundance at 1,000 W/R and 100 W/R from 10% Fe^{3+}/Fe_{tot} to 50% Fe^{3+}/Fe_{tot} at each modeled temperature. Summed in Table S7, there is a clear decrease in nontronite abundance with temperature and a significant increase at 100 W/R with increased Fe^{3+} availability. The chlorite abundance increases with temperature and decreases with Fe^{2+} availability (Table S9). The third group of clay minerals that formed in the models in this study was talc; for each modeled temperature, talc forms with increasing abundance from 10,000 – 1 W/R (Figures 5 and 6). Overall, talc abundance decreases with temperature and Fe^{2+} availability (Table S10).

Thermochemical modeling at 50 °C for the calculated alteration chemical compositions for the rocks below VRR and the overall Murray formation (Figure 7) returned near indistinguishable results at high W/R compared to the calculated chemical alteration composition for the rocks on VRR (Figures 5 and 6). This implies dominance of a hematite-clay mineral assemblage for high W/R over a range of environmental conditions.

To assess redox, all Fe- and S-bearing phases have to be taken into account. We note here that ferrous (including magnetite as a Fe-oxidation state mineral) and ferric minerals form at different W/R. The main influence on redox is expected from variations in the host rock chemical composition, especially in a subsurface system without access to atmospheric CO_2. While, as stated in the results section, the main silicate mineral composition remains largely unaffected by redox, there are differences in the hematite/sulfide ratio (Figures 5 and 6). Taking 75 °C as an example (Tables S5 and S6), 9.6 wt.% hematite and 10 wt.% pyrite precipitate from the system at 1,000 W/R and 10% Fe_{tot} as Fe^{3+}. In contrast, at 50% Fe_{tot} as Fe^{3+} in the host rock, the hematite/sulfide ratio increases from approximately 1 to 1.4 (12 wt.% hematite and 8.5 wt.% pyrite). However, at lower temperatures, and higher and lower W/R, the situation is different.

The pH for the models shown in this paper (Figures 5 and 6) at 10,000 W/R ranges from 7.9 to 9.3, as shown in Figure 8. At 10,000 W/R for the VRR Murray composition derived in Table S4, the pH trends from 9.4 to 8.0 for 25 to 100 °C at 10% Fe^{3+}/Fe_{tot} content and 9.2 to 7.9 for 25 to 100 °C at 50% Fe^{3+}/Fe_{tot} content. For pre-VRR Murray and overall Murray compositions in Table S4, the pH is 8.8 for 10% Fe^{3+}/Fe_{tot} content and the pH is 8.7 for 50% Fe^{3+}/Fe_{tot}. We attribute this increase in pH with decreasing W/R to H being consumed by phyllosilicate formation as increasing pH is commonly observed with decreasing W/R and increasing phyllosilicate formation (e.g., Schwenzer and Kring 2009, Bridges and Schwenzer, 2012; Bridges et al., 2015b).

5. Discussion

Our discussion first assesses the modeled mineral assemblages in context with the observations of the Murray formation. We then compare to other Martian-based models before looking at terrestrial comparisons.

5.1 Comparison of modeled mineral phases with Murray formation observations

The modeled early diagenetic mineral assemblages (Figures 5, 6 and 7) were compared to mineral phases observed by CheMin. To compare the modeled clay minerals to observations in the Murray formation, their chemistry is considered in section 5.3. Whilst the modeling method used in this study calculates chemical equilibrium at specific W/R, it is important to remember that low-temperature diagenetic processes are dominated by chemical kinetics (Misra, 2012). For this reason, we rely on comparisons with the ground truth – the observed mineralogy at VRR – for the setup of our model and the interpretation of our results. It is the combination of ground truth from the rover instruments with the models that allow us to arrive at our conclusions.

The abundances of Fe-oxides formed in the models varies with Fe^{3+}/Fe_{tot} content and, depending on temperature, speciation. Thermochemical models run at 25 °C do not compare well with *Curiosity* observations with regards to Fe-oxide abundance with clay (Tables 2 and 4), and as hematite, not goethite, is observed in the drilled samples (Achilles et al., 2020; Rampe et al., 2020b). As goethite can transform to hematite over time (Cornell and Schwertmann, 2006 *and references therein*) there is a possibility that these lower temperature models reflect the actual reaction pathway, and that the hematite-clay mineral assemblage observed in the Murray transformed from a goethite-clay mineral assemblage with burial and diagenesis of the sediments. It is important to note that, like goethite, ferrihydrite or magnetite may have also been precursors to the hematite observed in the Murray formation. This possibility is discussed by Achilles et al. (2020) for the hematite observed in Oudam and Rampe et al. (2020b) for the samples on VRR. The mechanisms to transform ferrihydrite to hematite include aqueous suspension under weakly acidic to weakly alkaline pH, and aging in a humid environment (Cornell and Schwertmann, 2006 *and references therein*). These mechanisms are discussed by Rampe et al. (2020b) for VRR with particular note on hematite crystallite size being an indicator for formation process. Magnetite was observed by *Curiosity* on VRR in Duluth, Stoer and Highfield (Rampe et al., 2020b), and is also a potential pre-cursor that can be transformed to hematite by oxidation. The magnetite chemistry was included in the chemical alteration compositions. Therefore, the models do not rule out the transformation of other Fe-oxides to hematite. However, in this study it is assumed that the present-day Fe-oxides observed in the Murray formation and VRR are what precipitated at the time of formation and have not since transformed, and so the thermochemical modeling results are compared to *Curiosity* observations.

Trace amounts of calcite, rhodochrosite, merwinite and spurrite were not included on the thermochemical model plots (Figures 5, 6 and 7). This is because the presence of phases such as spurrite ($Ca_5Si_2O_8(CO_3)$) and merwinite ($Ca_3MgSi_2O_8$) indicate a fluid rich in Ca. This is likely the result of Ca-sulfate contamination, which have been observed extensively in Gale crater (section 1). Trace amounts of carbonates such as calcite and rhodochrosite have not been observed with CheMin in the samples in this paper at the time of writing (January 2021). However, it has been indicated that siderite may be present in Rock Hall (Rampe et al., 2020b), and carbonates have been identified in SAM EGA data of samples from the Stimson formation

encountered earlier in the mission (Sutter et al., 2017). We note that it has been suggested, using an experimental approach on martian crust simulants, that carbonates only form when olivine is abundant and would not form in olivine-free assemblages under a CO_2 atmosphere (Baron et al., 2019).

The hematite/sulfide ratio is mainly controlled by the variation in the onset of nontronite formation (at systematically lower W/R with increasing temperature) under high-W/R conditions, and at low-W/R by the ratio of nontronite to celadonite as Fe-phyllosilicate phase. This demonstrates that the main redox sensitivity of such systems might not be discernible via the clay minerals alone. We note that phyllosilicates and their role in interpretation of the Mars samples is still being refined (Hurowitz et al., 2017; Bristow et al., 2018) and models suffer from uncertainties in the thermochemical data for these minerals (Catalano, 2013). Thus, it is encouraging to see that the system changes within strictly constrained boundaries of the input redox parameter conditions of the host rock.

5.2 Comparison of Modeled Mineral Abundances to those observed Murray Formation Mineralogy

For comparing the modeled mineral assemblages in this paper to observations made by *Curiosity*, we also considered the relative abundance of the observed altered phases. The observed CheMin clay mineral / Fe-oxide ratios in Table 4 are most comparable with the modeled ratios at 50 °C and 10,000 W/R shown in Tables 2 and 3, as also shown in Figure 9. Figure 9 shows that the observed CheMin ratios are not comparable with modeled clay mineral / Fe-oxide ratios at 50 °C for 1,000 or 100 W/R. Summing all Fe-oxides reported by CheMin significantly lowers the clay mineral / Fe-oxide ratio for the VRR mean ratio (Table 4), largely due to akaganeite in the Rock Hall drilled sample. As previously discussed, we note that akageneite might belong to a later alteration phase and formed independent of the hematite-clay mineral diagenetic environment where Fe is remobilized. In Figure 10, CheMin abundances of clay minerals and hematite are normalized to the calculated alteration component, which includes the composition of the amorphous component. The corresponding clay mineral and hematite abundances at 10,000 W/R from our thermochemical models at 50 °C reveal parallel negative correlations with CheMin samples Marimba, Sebina, Quela, Highfield and Oudam. Linear regression analysis revealed the comparability of these trends, with a gradient -2.35 ± 0.09 for the thermochemical models run at 50 °C and -1.88 ± 0.56 for Oudam, Marimba, Sebina, Quela, Duluth, Highfield and Rock Hall, with respective R^2 values of 0.99 and 0.70. The error associated with Duluth clay mineral and hematite abundance is within this negative correlation, so was included in the regression analyses. Rock Hall does not clearly align with this negative correlation, so to test whether it can be considered an outlier, linear regression was performed on Oudam, Marimba, Sebina, Quela, Duluth and Highfield, which revealed a gradient of -2.56 ± 0.45 with an R^2 value of 0.89. The improvement of the fit confirms that Rock Hall can be considered an outlier, which is further suggestive of alteration after the initial hematite-clay mineral main phase alteration modeled in this paper. In Figure 10, the position of Stoer relative to negative correlation of clay minerals and hematite in Marimba, Sebina, Quela, Highfield and Oudam is comparable to the position of the thermochemical models run at 50 °C relative to those run at higher temperature (75 °C and 100 °C). This shows a possible increase in temperature for the formation of the main phase alteration mineral assemblage in Stoer.

The plotted data in Figure 10 also show that, although the bulk alteration composition used in the thermochemical models varies to a relatively minor extent (Table S4), such small variations impact the precipitated amounts of clay minerals and hematite in the thermochemical model results. However, this variation in modeled mineral abundance corresponds to modeled CheMin secondary mineral abundance. In Figure 10, the shift between the trend in the CheMin detections and the trend in the thermochemical models raises the question of the role of the CheMin amorphous component, as chemical contributions from the amorphous component detected by APXS were included in the chemical alteration compositions used in the thermochemical modeling.

Here we assume the amorphous component includes sample constituents that cannot be identified from CheMin data because crystalline materials in the samples below 1 wt.% are included in the amorphous component. The composition of this amorphous composition is estimated using CheMin-APXS FULLPAT analysis (Rampe et al., 2020b; Achilles et al., 2020). The origin of the X-ray amorphous component is presently not fully understood. However, studies have indicated the presence of nanophase Fe-oxides, amorphous sulfates, silicates and low amounts of basaltic glass in the amorphous component (Bish et al., 2013; Smith et al., 2019; Rapin et al., 2019; Rampe et al., 2020a). A study by Bridges et al (2015b), where Portage soil was used in the starting composition, assumed that the amorphous component contained volcanic or impact glass, which was then reacted together with olivine to successfully model the alteration assemblages observed at Yellowknife Bay. As mentioned in section 1.1, the amorphous composition is high in Fe and Si, suggesting the presence of nanophase Fe-oxides and amorphous silica in the sedimentary rock (Rampe et al., 2020a; Achilles et al., 2020). Considering the models presented in this paper assume that all mineralogy is essentially crystalline, the linear shift between modeled and observed trends in Figure 10 could be attributed to an unreacted component of the calculated alteration composition in the drill samples. The Marimba, Quela, Sebina, Highfield and Stoer mineral abundances are clustered close to the thermochemical models run with their alteration compositions. As previously noted, the position of Stoer is comparable to higher temperature (75 °C and 100 °C) thermochemical models.

We tested the idea that the amorphous component might only partially belong to the alteration materials by removing the amorphous component from the CheMin mineral abundances for each drill hole and re-normalizing. This improves the fit between thermochemical model results and CheMin observations with regards to the negative correlation between hematite and clay mineral abundances (Figure 11). Although there are comparable negative correlations, albeit of different gradients, between the drilled samples analysed by CheMin and the thermochemical models in Figure 11, the trend with temperature shown in Figure 10 is lost. This suggests that a part of the amorphous component is reactive. We hypothesize that the CheMin alteration composition was not fully reacted during this phase of alteration. Therefore, this could suggest that the amorphous component had a reactive component and a non-reactive component or that time was insufficient to fully react the amorphous component. The latter could be indicative of the alteration of a volcanic glass (e.g. Wolff-Boenisch et al., 2004). Considering the modeling method assumes complete host rock dissolution and igneous phases are still present in *Curiosity* observations, an unreacted igneous glass component is favored here.

5.3 Clay Minerals and Comparisons to Yellowknife Bay and other Martian terrains, including the Nakhlite Martian Meteorites

The results of this work can be compared to earlier theoretical modeling involving general Martian compositions deduced from Martian meteorite compositions (e.g., Schwenzer and Kring, 2009; Filiberto and Schwenzer, 2013), the composition of rocks at Yellowknife Bay in Gale crater (Bridges et al., 2015b; Schwenzer et al., 2016), and the nakhlite Martian meteorite alteration (Bridges and Schwenzer, 2012). Those models are based on varying knowledge of the reaction path, with general assumptions on the alteration paragenesis from orbiters for the first set of models, more precise knowledge of alteration mineral occurrence from CheMin at Yellowknife Bay, and finally a detailed investigation of the alteration assemblage in the nakhlite meteorites. Our study is comparable to the Yellowknife Bay study (Bridges et al., 2015b) in the level of knowledge of the alteration assemblage, and comparisons between the Yellowknife Bay Sheepbed member of the Bradbury Group and the Murray formation are particularly important in understanding the evolution of fluids in the Gale crater sediments. The dioctahedral nontronite in our models is a close analogy to the dioctahedral smectite identified in Murray (Bristow et al., 2018), therefore our models have identified a possible diagenetic process to form the hematite-clay mineral assemblage in the Murray formation. The phyllosilicate-bearing assemblage analyzed in the Gale sediments contains no serpentine, chlorite and, at most, traces of illite (Bristow et al., 2018; Rampe et al., 2020b). Phyllosilicates are widespread in the Murray formation and, when present, dominated by smectites.

We start by comparing our assemblage to general Martian alteration deduced from orbiter observations and the MER rovers. The basis for these models were Martian meteorite compositions, e.g., LEW88516 for the models presented by Schwenzer and Kring (2009). Based on this poikilitic shergottite composition, the models are dominated by forsteritic olivine (57 vol.%, with contributions from pyroxene (22 vol.%) and plagioclase (16 vol.%) (Gleason et al., 1997). These models showed that there are two important observations: nontronite – which is observed from orbit (Ehlmann et al., 2009; Miliken et al., 2010; Carter et al., 2013) and used as the anchor point for this study – most frequently occurs at intermediate temperatures (~150 °C) and is replaced by chlorite and eventually amphiboles at the higher temperatures of up to 350 °C. At lower temperatures (<90 °C) the dominance of forsteritic olivine causes talc formation to become more dominant. The system is, however, multi-dimensional, as W/R also influences the assemblage, with nontronite generally dominant around W/R of 1,000, being replaced by other phyllosilicates and eventually amphiboles towards lower W/R. At the highest W/R (e.g. 10,000) hematite dominates, with some nontronite. The results are similar to the results of this study focusing on the Murray formation of Gale crater in the comparable pattern of hematite dominance at the highest W/R. They differ in the occurrence of talc at the lower temperatures, which can be explained by the difference between LEW88516 and our calculated alteration compositions for the Murray formation in the MgO concentration (24 wt.% for LEW88516) (Schwenzer and Kring, 2009) vs. 5 wt.% (Table S4). This highlights the importance of host rock composition for the alteration mineral formation, along with the effect of temperature and different W/R ratios. The importance of host rock composition is also highlighted by the fact that models with ‘Home Plate’ MER Spirit rock ‘Fastball’ composition form nontronite at temperatures as low as 13 °C (Filiberto and Schwenzer, 2013). Filiberto and Schwenzer (2013) hypothesized that 13 °C was the temperature at 1 km depth if the surface temperature is zero and the Martian geothermal gradient is 13 °C (Babeyko and Zharkov, 2000). MgO concentration in the assumed host rock is 12 wt.%, significantly lower than for LEW88516, but higher than in this

study. MgO/Al_2O_3 ratios are 7.6 for LEW88516, 1.5 for Fastball, and 0.97 for the models in this study (Table S4). This significantly influences the stability of talc compared to nontronite, but also the W/R at which the transition between nontronite and chlorite occurs. Those studies (Filiberto and Schwenzer, 2013) were based on well-known host rock compositions, but for the Gusev alteration mineral assemblage only orbiter data could be used.

Previous modeling for the Sheepbed unit (Bridges et al., 2015b) was based on Portage Soil with 13 wt% MgO, and an MgO/Al_2O_3 ratio of 0.92 (Blake et al., 2013). Clay minerals formed in the first stage of the model, because sulfate minerals were only observed in later veins (Bridges et al., 2015b; Schwenzer et al., 2016). The models showed that the secondary mineral assemblage formed by the reaction of a CO_2-poor and moderately oxidizing, dilute aqueous solution with the sedimentary rocks at 10–50°C and W/R of 100–1,000, pH of ~7.5–12 (but mainly near neutral through most of the reaction range). Modeled phyllosilicates were Fe-smectite and chlorite. The bulk phyllosilicate composition was close to saponite stoichiometry, which is inferred from CheMin data (Vaniman et al., 2014) though more Fe-rich than the bulk clay mineral composition predicted here for the Murray formation at high W/R (Figure 12).

The nakhlite meteorite alteration assemblage's reaction pathways were assessed in a different way (Bridges and Schwenzer, 2012), because both the host rock and the alteration assemblage are known to a high level of detail, including precipitation and re-dissolution successions (e.g. Hicks et al., 2014; Bridges et al., 2019). As a consequence of that knowledge, the host rock composition could be adapted to match differences in dissolution of individual mineral phases. The model concentration has 9 wt.% MgO, and the MgO/Al_2O_3 ratio is 1.9. Furthermore, the observations of the alteration mineral succession in the meteorites indicated a two-step process, carbonate formation first, followed by the silicate-forming phase. This caused a change in the fluid during mineral precipitation, with the silicate-stage fluid being enriched in Si, Na, Al, and K. Taking this into account, Fe-smectites form over a wide range of W/R down to 100 W/R or as low as 10 W/R (Bridges and Schwenzer, 2012). This study on Martian meteorites demonstrates the importance in the accuracy of reaction pathway models presented here for observations on the nature of the alteration phase, as well as any indication of differences in alteration conditions for different stages of alteration.

For the Sheepbed mudstone of the Bradbury Group there exists the same level of detailed mineralogical knowledge on pre and post alteration mineralogy as we have for the VRR-Murray formation rocks. CheMin X-ray diffraction patterns and SAM evolved gas analyses from mudstone samples demonstrate that phyllosilicate types and abundances vary within the stratigraphic section. Abundant (~20 wt.% of the bulk) Fe^{3+}-bearing saponite (a trioctahedral smectite) was identified in mudstone from the Yellowknife Bay formation at the base of the section (Treiman et al., 2014; Vaniman et al., 2014). Mudstone from the Pahrump Hills member, ~60 m up section from Yellowknife Bay and at the base of the Murray formation, has little to no phyllosilicate (up to 8 wt.% of the bulk), and CheMin XRD patterns are consistent with the presence of collapsed smectite (Rampe et al., 2017). Much of the Murray formation stratigraphically above the Pahrump Hills member has abundant (up to 28 wt.% of the bulk) collapsed smectite (Bristow et al., 2018). Both CheMin and SAM data suggest that the structure of the smectite changes from being dominantly trioctahedral (i.e., saponite) lower in the section to being dominantly dioctahedral (i.e., montmorillonite and/or nontronite) higher in the section (Bristow et al., 2018). Duluth was the first sampled analyzed by *Curiosity* to clearly contain only dioctahedral smectite (nontronite, in this case) (Rampe et al., 2020b; McAdam et al., 2020).

Phyllosilicates on VRR are distinctly different from those detected in mudstone stratigraphically below the ridge. The abundance of phyllosilicates on VRR is relatively low compared to much of the Murray formation (e.g., Highfield contains 5 wt.% phyllosilicate) (Rampe et al., 2020b). Based on our models, this decrease in phyllosilicates likely relates to the aqueous alteration environment being more oxidizing on the VRR relative to that below (Figure 10). Furthermore, the phyllosilicates on VRR show a 9.6 Å basal spacing, rather than a 10 Å basal spacing observed in nearly all other phyllosilicate-bearing XRD patterns. This suggests that the phyllosilicate is either a completely collapsed smectite, possibly from alteration in acidic fluids, or that the phyllosilicate is a non-expanding clay mineral, like ferripyrophyllite. SAM data are also consistent with completely collapsed nontronite or ferripyrophyllite on VRR. A similar phyllosilicate was observed in very low abundances in the Oudam sample, drilled stratigraphically above the Pahrump Hills member (Bristow et al., 2018), and the mineralogical similarities between Oudam and Highfield from the gray Jura suggest a comparable aqueous alteration history, as also suggested by our model results (Figure 10). However, Bristow et al. (2018) hypothesized a detrital origin for ferripyrophyllite at Oudam.

There is a notable similarity in trioctahedral saponite observed in Sheepbed mudstone (Vaniman et al., 2014) and the phyllosilicate identified in the nakhlite martian meteorites. Some of these 11 meteorites contain ferric saponite with a trioctahedral structure (Hicks et al., 2014). Trioctahedral saponite as an alteration product of Martian mafic material can be regarded as one of the expected types. Fe/Mg smectites, whether tri or dioctahedral have been identified in numerous places from orbit by reflectance spectroscopy (e.g. Ehlmann et al., 2011; Bibring et al, 2006). In the thermochemical models presented in this paper for the Murray formation, the dioctahedral clay nontronite is dominant at W/R up to 10,000 (Figures 5, 6 and 7). Similar to the Gale *in situ* analyses, serpentine is absent and chlorite is only dominant at extreme W/R, >10,000 in our models. The slightly elevated temperatures of the models in this study (50–100 °C) compared to thermochemical modeling for Yellowknife Bay (10–50 °C; Bridges et al., 2015b), suggests that the fluids may have been sourced from deep, warm aquifers. To further compare the results of this study to previous works, we have summed the phyllosilicate chemical composition for the models in this paper and included them on a ternary plot in Figure 12, with comparisons to previous modelling at Yellowknife Bay (Bridges et al., 2015b) and martian meteorite studies (Hicks et al., 2014). As shown in Figure 12, the modeled phyllosilicates at W/R 10,000 in this study are close to observed Fe-saponites from the nakhlites (Lafayette) and Sheepbed unit model saponite (Bridges et al., 2015b). Murray formation modeling in this paper at 1,000 and 100 W/R trend towards a nontronite composition, as shown in Figure 12.

5.4 Comparison to alteration processes in terrestrial environments

Impact-craters are long recognized as depressions in which lakes, and sediments, accumulate (Cabrol and Grin, 1999; Osinski et al., 2013). Gale crater is no exception, as recognized early in the MSL mission and ever since, *Curiosity* is exploring a rich stratigraphy of lakebed sediments (e.g., Edgar et al., 2020; Fedo et al., 2018; Grotzinger et al., 2014, 2015; Hurowitz et al., 2017; section 1). Our hypothesis is that the clay-hematite assemblage is predominantly the result of the first phase of diagenetic alteration that affected the sediments brought into Gale crater. The sedimentary textures within Gale crater, such as cross-bedding, and coarser units such as conglomerates (Williams et al., 2013; section 1) thereby support the assumption of a dynamic environment with freshwater inflow. This underpins our assumption of a dilute, circumneutral 'groundwater-type' fluid as the initial pore fluid. The main difference

between most of those settings and terrestrial analogues is, unfortunately, one of host rock composition as most of Earth's examples are in more evolved rocks and/or less iron-rich than the compositionally-basaltic sequences at Gale crater.

Several terrestrial impact craters show sedimentary sequences of lake bed characteristics, starting with coarse grained sequences gradually transitioning to finer grained sequences, but with considerable variation and cyclicity, e.g., the Gardnos impact structure in Norway (Kalleson et al., 2008) and the Boltysh impact structure in the Ukraine (Gilmour et al., 2013). The 14.808 ± 0.021 Ma (Schmieder et al., 2018), 24 km diameter Ries impact Crater (Nördlingen, Germany) has been compared to Gale crater (Arp et al., 2019) as it contains a succession of lake bed sediments and is a closed basin. Interestingly, the transport distances for conglomerates at Ries are considered to be short due to impact-pre-processing (Arp et al., 2019). The sequence begins with clastic sediments with conglomerates and evidence of cyclicity including variation in geochemical properties of the lake (oxygen fugacity, salinity, acidity, and new freshwater inflow; Jankowski, 1977; Arp et al., 2013), which is similar to observations at Gale of fan deposit formation (Williams et al., 2013) and a complex lake chemistry (Hurowitz et al., 2017). This shows that sedimentation was accompanied by significant quantities of water, and therefore a groundwater-type scenario as assumed in our study is plausible. Alteration mineralogy of the original target rock is consistent with a low-temperature alteration process (Muttik et al., 2008), whereby clays are montmorillonite-type smectites. This is comparable to our findings of nontronite, as the difference in clay minerals reflects the chemical differences of the host rock: gneiss fragments dominated by feldspars at Ries crater, basaltic sediments dominated by mafic phases and plagioclase at Gale crater. The higher Fe-content of the rocks at Gale crater, 23-30 wt.% (Table S2), compared to the Ries basement rocks, 2-9 wt.% (von Engelhardt, 1997), explains the different clay mineral chemistry but maintains the low-temperature, groundwater-driven clay formation environmental conditions.

We next compare to a setting more comparable in chemistry while noting that Fe-concentrations at VRR are still higher than those of most terrestrial basalts; Lonar crater (Hagerty and Newsom, 2003) and the basalt alteration widely observed in the Deccan trap basalts. In the Northeastern part of the Deccan Traps, near Jabalpur, unweathered basalts generally contain between 11 and 15 wt.% FeO_{tot} (Peng et al., 1998). Investigation of sedimentary and weathered basalt samples by Salil et al. (1997) in the same region near Jabalpur show that clay minerals have a similar FeO_{tot} content compared to the basalts: between 10 and 17 wt.% with a dominance of Fe_2O_3. Iron concentrations between rock and alteration assemblage appear constant, if not slightly higher in the sediments and basaltic alteration assemblages, which is comparable to our observations where Fe in the fluid is generally very low (~10^{-9}) at 10,000 W/R (Figure S1). For the Deccan Traps, Fe-concentrations in runoff water of the region appear comparably very low as they are not reported for the region (Gupta et al., 2011), or more widely in cold and warm spring waters as well as runoff across the Deccan (Minissale et al., 2000). Clay-mineralogy in the sediments and Deccan alteration is Fe, Mg-rich smectites, which the authors describe as similar to but not quite nontronitic as the Fe-content is below 50% (Salil et al., 1997). This shows that water-dominated, groundwater-rock reactions such as proposed here occur in weathering or diagenetic environments and are similar to the observed clay mineralogy at the Gale site and in our models.

6. Conclusions

In this paper we showed that local element mobility rather than large scale, basin-wide fluid movement is the most likely alteration mechanism for the main phase of alteration in the Murray formation. For this, we derived chemical alteration compositions using data from CheMin (Achilles et al., 2020; Rampe et al., 2020b) and APXS (Thompson et al., 2020) and found them to be very similar for the Murray formation below as well as on Vera Rubin ridge. After this main phase, based on the age dating and the local nature of its occurrence, a younger alteration event caused the observed akaganeite and jarosite, whereby we assume that Fe was remobilized from the mineral assemblages in our models (i.e. Fe-sulfides).

Our thermochemical modeling results indicate that the alteration that produced the early diagenetic hematite-clay mineral assemblage in the Murray formation, below and on VRR, can be explained by reaction of dilute brine with the calculated alteration compositions at temperatures between 50 and an upper limit of 100 °C, and at a notably high W/R of approximately 10,000 with pH ranging from 7.9 to 9.3. Modeling at 25 °C produces goethite, which could transition to hematite at a later stage however, this phase together with the relative abundances with the clay content are not directly comparable to *Curiosity* observations. We interpret the high W/R as enhanced groundwater flow through this part of the Gale sedimentary sequence compared to that in the Bradbury Group and its Yellowknife Bay mudstone.

The trends between the modeled and observed phyllosilicate and hematite abundances are comparable, but not exact due to our model not precipitating metastable phases such as the CheMin amorphous component. We interpret the amorphous component to have partially contributed to the phase of alteration modeled in this study. Future work is necessary to determine the composition and origin of the CheMin amorphous component, and thus how its chemistry can be most appropriately used in thermochemical modeling studies. We will continue modeling the Gale crater sedimentary mineral assemblage which in future work we aim to extend from the Bradbury and Murray-VRR, into the clay-bearing Glen Torridon and overlying Sulfate Units.

Acknowledgments, Samples, and Data

SMRT, SPS and JCB were funded by UK Space Agency grant ST/S001522/1. CCB was funded through the STFC doctoral training grant to the OU. ACM acknowledges funding support from the NASA ROSES MSL Participating Scientist Program. Unless stated otherwise, mineralogical and chemical data used in the modeling from the Mars Science Laboratory *Curiosity* rover are from the NASA PDS. Data necessary to reproduce the thermochemical modeling results shown in this paper will be available on The Open University data repository (https://ordo.open.ac.uk/). Authors would like to thank Jim Palandri for CHIM-XPT access and support. Support from the scientists, engineers, colleagues in operations roles, and staff of NASA Mars Science Laboratory Mission is gratefully acknowledged. SMRT would like to thank Nisha Ramkissoon for thermochemical modeling discussions. Previous versions of this manuscript benefitted from reviews by Benjamin Tutolo, Jake Crandall, and three anonymous reviewers.

References

Achilles C.N., Rampe E.B., Downs R.T., Bristow T.F., Ming D.W., Morris R.V., Vaniman D.T., Blake D.F., Yen A.S., McAdam A.C., Sutter B., Fedo C.M., Gwizd S., Thompson L.M., Gellert R., Morrison S.M., Treiman A.H., Crisp J.A., Gabriel T.S.J., Chipera S.J., Hazen R.M., Craig P.I., Thorpe M.T., Des Marais D.J., Grotzinger J.P., Tu V.M., Castle N., Downs G.W., Peretyazhko T.S., Walroth R.C., Sarrazin P., and Morookian J.M. 2020. Mineralogy of ancient fluvial-lacustrine sediments in Gale crater, Mars: Evidence for multiple diagenetic episodes. Journal of Geophysical Research: Planets, 125, e2019JE006295.

Anderson R.B., and Bell III, J.F. 2010. Geologic mapping and characterization of Gale Crater and implications for its potential as a Mars Science Laboratory landing site. Mars 5, 76-128.

Arp G., Schultz S., Karius V., and Head III J.W. 2019. Ries impact crater sedimentary conglomerates: Sedimentary particle'impact pre-processing', transport distances and provenance, and implications for Gale crater conglomerates, Mars. Icarus, 321, pp.531-549.

Babeyko A.Y., and Zharkov V.N. 2000. Martian crust: a modeling approach. Physics of the Earth and planetary interiors, 117(1-4), 421-435.

Baron F., Gaudin A., Lorand J.P., and Mangold N. 2019. New Constraints on Early Mars Weathering Conditions from an Experimental Approach on Crust Simulants. Journal of Geophysical Research: Planets, 124, 1783-1801.

Bedford C.C., Bridges J.C., Schwenzer S.P., Wiens R.C., Rampe E.B., Frydenvang J., and Gasda P.J. 2019. Alteration trends and geochemical source region characteristics preserved in the fluviolacustrine sedimentary record of Gale crater, Mars. Geochemica et Cosmochimica Acta, 246, 234-266. doi:10.1016/j.gca.2018.11.031.

Bennett K.A., Edgett K., Fey D., Edgar L.A., Fraeman A., McBride M., and Edwards C. 2018. Fine-Scale Textural Observations at Vera Rubin Ridge, Gale Crater, from the Mars Hand Lens Imager (MAHLI). In Proceedings 49th Lunar and Planetary Science Conference, The Woodlands, TX (Vol. 49, p. 1769).

928 Blake D.F., Morris R.V., Kocurek G., Morrison S.M., Downs R.T., Bish D., Ming D.W., Edgett
929 K.S., Rubin D., Goetz W., Madsen M.B., Sullivan R., Gellert R., Campbell I., Treiman
930 A.H., McLennan S.M., Yen A.S., Grotzinger J., Vaniman D.T., Chipera S.J., Achilles
931 C.N., Rampe E.B., Sumner D., Meslin P.-Y., Maurice S., Forni O., Gasnault O., Fisk M.,
932 Schmidt M., Mahaffy P., Leshin L.A., Glavin D., Steele A., Freissinet C., Navarro-
933 González R., Yingst R.A., Kah L.C., Bridges N., Lewis K.W., Bristow T.F., Farmer J.D.,
934 Crisp J.A., Stolper E.M., Des Marais D.J., Sarrazin P., and MSL Science Team 2013.
935 Curiosity at Gale crater, Mars: Characterization and analysis of the Rocknest sand
936 shadow. Science, 341(6153), p.1239505.

937 Blake D., Vaniman D., Achilles C., Anderson R., Bish D., Bristow T., Chen C., Chipera S., Crisp
938 J., Des Marais D., Downs R.T., Farmer J., Feldman S., Fonda M., Gailhanou M., Ma H.,
939 Ming D.W., Morris R.V., Sarrazin P., Stolper E., Treiman A., and Yen A. 2012.
940 Characterization and calibration of the CheMin mineralogical instrument on Mars
941 Science Laboratory. Space Sci. Rev. 170(1-4), 341-399.

942 Bibi I., Singh B., and Silvester E. 2011. Akaganéite (β-FeOOH) precipitation in inland acid
943 sulfate soils of south-western New South Wales (NSW), Australia. Geochimica et
944 Cosmochimica Acta, 75(21), 6429-6438.

945 Bibring J.P., Langevin Y., Mustard J.F., Poulet F., Arvidson R., Gendrin A., Gondet B., Mangold
946 N., Pinet P., Forget F., and the OMEGA team 2006. Global mineralogical and aqueous
947 Mars history derived from OMEGA/Mars Express data. Science, 312(5772), 400-404.

948 Bish D.L., Blake D.F., Vaniman D.T., Chipera S.J., Morris R.V., Ming D.W., Treiman A.H.,
949 Sarrazin P., Morrison S.M., Downs R.T., Achilles C.N., Yen A.S., Bristow T.F., Crisp
950 J.A., Morookian J.M., Farmer J.D., Rampe E.B., Stolper E.M., Spanovich N., and MSL
951 Science Team 2013. X-ray diffraction results from Mars Science Laboratory: Mineralogy
952 of Rocknest at Gale crater. Science, 341(6153), p.1238932.

953 Bridges J.C., and Schwenzer S.P. 2012. The nakhlite hydrothermal brine on Mars. Earth and
954 Planetary Science Letters, 359, 117-123.

955 Bridges J.C., Schwenzer S.P., Leveille R., Wiens R.C., McAdam A., Conrad P., and Kelley S.P.
956 2015a. Hematite Formation in Gale Crater. In Lunar and Planetary Science Conference,
957 The Woodlands, TX (Vol. 46, p. 1769).

958 Bridges J.C., Schwenzer S.P., Leveille R., Westall F., Wiens R.C., Mangold N., Bristow T.,
959 Edwards P., and Berger G. 2015b. Diagenesis and Clay mineral Formation in Gale
960 Crater, Mars. J. Geophys. Res. Planets, 120, 1-19, doi:10.1002/2014JE004757.

961 Bridges J.C., Hicks, L.J., and Treiman A.H. 2019. Carbonates on Mars. In Volatiles in the
962 Martian Crust. 1st edition. Elsevier. Editors Filiberto and Schwenzer, pp 426.

963 Bristow T.F., Rampe E.B., Achilles C.N., Blake D.F., Chipera S.J., Craig P., Crisp J.A., Des
964 Marais D.J., Downs R.T., Gellert R., Grotzinger J.P., Gupta S., Hazen R.M., Horgan B.,
965 Hogancamp J.V., Mangold N., Mahaffy P.R., McAdam A.C., Ming D.W., Morookian
966 J.M., Morris R.V., Morrison S.M., Treiman A.H., Vaniman D.T., Vasavada A.R., and
967 Yen, A.S. 2018. Clay mineral diversity and abundance in sedimentary rocks of Gale
968 crater, Mars. Science Advances (6), eaar3330.

Cabrol N.A., and Grin E.A. 1999. Distribution, classification, and ages of Martian impact crater lakes. Icarus, 142(1), pp.160-172.

Carter J., Poulet F., Bibring J.P., Mangold N., and Murchie S. 2013. Hydrous minerals on Mars as seen by the CRISM and OMEGA imaging spectrometers: Updated global view. Journal of Geophysical Research: Planets, 118(4), 831-858.

Catalano J.G. 2013. Thermodynamic and mass balance constraints on iron-bearing phyllosilicate formation and alteration pathways on early Mars. Journal of Geophysical Research: Planets, 118(10), 2124-2136.

Catling D.C., and Moore J.M. 2003. The nature of coarse-grained crystalline hematite and its implications for the early environment of Mars. Icarus, 165(2), 277-300, http://dx.doi.org/10.1016/S0019-1035(03)00173-8.

Chevrier V., Poulet F., and Bibring J.-P. 2007. Early geochemical environment of Mars as determined from thermodynamics of phyllosilicates. Nature, **448**: 60–63.

Cornell and Schwertmann 2006. The Iron Oxides: Structure, Properties, Reactions, Occurrences and Uses, John Wiley & Sons.

Deer W.A., Howie R.A., and Zussman J. 1992. An introduction to the rock-forming minerals. 2nd edition. The Mineralogical Society, London.

Deer W.A., Howie R.A., and Zussman J. 2013. An introduction to the rock-forming minerals. 3rd edition. The Mineralogical Society, London.

Edgar L.A., Fraeman A., Gupta S., Fedo C., Grotzinger J.P., Stack K., Bennett K.A., Sun V.Z., Banham S., Stein N., Edgett K.S., Rubin D.M., House C.H., and Van Beek J. 2018. A Lacustrine Environment Recorded at Vera Rubin Ridge: Overview of the Sedimentology and Stratigraphy observed by the Mars Science Laboratory Curiosity Rover. In Proceedings AGU, Washington, D.C.

Edgar L.A., Fedo C.M., Gupta S., Banham S.G., Fraeman A.A., Grotzinger J.P., Stack K.M., Stein N.T., Bennett K.A., Rivera-Hernández F., Sun V.Z., Edgett K.S., Rubin D.M., House C., and van Beek J. 2020. A lacustrine paleoenvironment recorded at Vera Rubin ridge, Gale crater: Overview of the sedimentology and stratigraphy observed by the Mars Science Laboratory Curiosity rover. Journal of Geophysical Research: Planets, 125, e2019JE006307.

Ehlmann B.L., Mustard J.F., Swayze G.A., Clark R.N., Bishop J.L., Poulet F., Des Marais D.J., Roach L.H., Milliken R.E., Wray J.J., Barnouin-Jha O., and Murchie S.L. 2009. Identification of hydrated silicate minerals on Mars using MRO-CRISM: Geologic context near Nili Fossae and implications for aqueous alteration. Journal of Geophysical Research: Planets, 114(E2).

Ehlmann B.L., Mustard J.F., Murchie S.L., Bibring J.P., Meunier A., Fraeman A.A., and Langevin Y. 2011. Subsurface water and clay mineral formation during the early history of Mars. Nature, 479(7371), 53.

Filiberto J., and Schwenzer S.P. 2013. Alteration mineralogy of Home Plate and Columbia Hills—Formation conditions in context to impact, volcanism, and fluvial activity. Meteoritics & Planetary Science, 48(10), 1937-1957.

Fraeman A.A., Arvidson R.E., Catalano J.G., Grotzinger J.P., Morris R.V., Murchie S.L., Stack K.M., Humm D.C., McGovern J.A., Seelos F.P., Seelos K.D., and Viviano C.E. 2013. A hematite-bearing layer in Gale Crater, Mars: Mapping and implications for past aqueous conditions. Geology, 41(10), 1103-1106.

Fraeman A.A., Ehlmann B.L., Arvidson R.E., Edwards C.S., Grotzinger J.P., Milliken R.E., Quinn D.P., and Rice M.S. 2016. The Stratigraphy and Evolution of Lower Mt. Sharp from Spectra, Morphological, and Thermophysical Orbital Datasets. Journal of Geophysical Research: Planets, 121(9), 1713-1736.

Fraeman A.A., Edgar L.A., Rampe E.B., Thompson L.C., Frydenvang J., Fedo C., Catalano J.G., Dietrich W.E., Gabrie, T.S.J., Vasavada A.R., Grotzinger J.P., L'Haridon J., Mangold N., Sun V.Z., House C.H., Bryk A.B., Hardgrove C., Czarnecki S., Stack K.M., Morris R.V., Arvidson R.E., Banham S.G., Bennett K.A., Bridges J.C., Edwards C.S., Fischer W.W., Fox V.K., Gupta S., Horgan B.H.N., Jacob S.R., Johnson J.R., Johnson S.S., Rubin D.M., Salvatore M.R., Schwenzer S.P., Siebach K.L., Stein N.T., Turner S.M.R., Wellington D.F., Wiens R.C., Williams A.J., David G., and Wong G.M. 2020. Evidence for a Diagenetic Origin of Vera Rubin Ridge, Gale Crater, Mars: Summary and Synthesis of *Curiosity's* Exploration Campaign. Journal of Geophysical Research: Planets, 125, e2020JE006527.

Frydenvang J., Gasda P.J., Hurowitz J.A., Grotzinger J.P., Wiens R.C., Newsom H.E., Edgett K.S., Watkings J., Bridges J.C., Maurice S., Fisk M.R., Johnson J.R., Rapin W., Stein N.T., Clegg S.M., Schwenzer S.P., Bedford C.C., Edwards P., Mangold N., Cousin A., Anderson R.B., Payré V., Vaniman D., Blake D.F., Lanza N.L., Gupta S., Van Beek J., Sautter V., Meslin P.-Y., Rice M., Milliken R., Gellert R., Thompson L., Clark B.C., Sumner D.Y., Fraeman A.A., Kinch K.M., Madsen M.B., Mitrofanov I.G., Jun I., Calef F., and Vasavada A.R. 2017. Diagenetic silica enrichment and late-stage groundwater activity in Gale crater, Mars. Geophysical Research Letters, 44(10), 4716-4724.

Frydenvang J., Mangold N., Wiens R.C., Fraeman A.A., Edgar L.A., Fedo C., L'Haridon J., Bedford C.C., Gupta S., Grotzinger J.P., Bridges J.C., Clark B.C., Rampe E.B., Gasnault O., Maurice S., Gasda P.J., Lanza N.L., Olilla A.M., Meslin P.-Y., Payré V., Calef F., Salvatore M., and House C.M. 2020. The Chemostratigraphy of the Murray Formation and Role Of Diagenesis at Vera Rubin Ridge in Gale Crater, Mars, as Observed by the ChemCam Instrument. Journal of Geophysical Research: Planets, 125, e2019JE006320.

Ganguly J. 2008. Thermodynamics in Earth and Planetary Science. Springer. Berlin-Heidelberg. 501 p.

Gilmour I., Jolley D.W., Watson J. S., Gilmour M. A., and Kelley S. P. 2013. Post-impact heating of a crater lake. In: European Planetary Science Congress 2013, 08-13 Sep 2013, London.

Gleason J.D., Kring D.A., Hill D.H., and Boynton W.V. 1997. Petrography and bulk chemistry of Martian lherzolite LEW88516. Geochimica et Cosmochimica Acta, 61(18), 4007-4014.

Griffith L.L., and Shock E.L. 1995. A geochemical model for the formation of hydrothermal carbonates on Mars. Nature, **377**: 406–408.

Griffith L.L., and Shock E.L., 1997. Hydrothermal hydration of Martian crust: Illustration via geochemical model calulations. Journal of Geophysical Research, **102**: 9135–9143.

Grotzinger J.P., Sumner D.Y., Kah L.C., Stack K., Gupta S., Edgar L., Rubin D., Lewis K., Schieber J., Mangold N., Milliken R., Conrad P.G., DesMarais D., Farmer J., Siebach K., Calef III F., Hurowitz J., McLennan S.M., Ming D., Vaniman D., Crisp J., Vasavada A., Edgett K.S., Malin M., Blake D., Gellert R., Mahaffy P., Wiens R.C., Maurice S., Grant J.A., Wilson S., Anderson R.C., Beegle L., Arvidson R., Hallet B., Sletten R.S., Rice M., Bell III J., Griffes J., Ehlmann B., Anderson R.B., Bristow T.F., Dietrich W.E., Dromart G., Eigenbrode J., Fraeman A., Hardgrove C., Herkenhoff K., Jandura L., Kocurek G., Lee S., Leshin L.A., Leveille R., Limonadi D., Maki J., McCloskey S., Meyer M., Minitti M., Newsom H., Oehler D., Okon A., Palucis M., Parker T., Rowland S., Schmidt M., Squyres S., Steele A., Stopler E., Summons R., Treiman A., Williams R., Yingst A., and MSL Science Team 2014. A Habitable Fluvio-Lacustrine Environment at Yellowknife Bay, Gale Crater, Mars. Science, 343(6169), p.1242777.

Grotzinger J.P., Gupta S., Malin M.C., Rubin D.M., Schieber J., Siebach K., Sumner D.Y., Stack K.M., Vasavada A.R., Arvidson R.E., Calef III F., Edgar L., Fischer W.F., Grant J.A., Griffes J., Kah L.C., Lamb M.P., Lewis K.W., Mangold N., Minitti M.E., Palucis M., Rice M., Williams R.M.E., Yingst R.A., Blake D., Blaney D., Conrad P., Crisp J., Dietrich W.E., Dromart G., Edgett K.S., Ewing R.C., Gellert R., Hurowitz J.A., Kocurek G., Mahaffy P., McBride M.J., McLennan S.M., Mischna M., Ming D., Milliken R., Newson H., Oehler D., Parker T.J., Vaniman D., Wiens R.C., and Wilson S.A. 2015. Deposition, exhumation, and paleoclimate of an ancient lake deposit, Gale crater, Mars. Science, v. 350, no. 6257, p. aac7575.

Gupta H., Chakrapani G.J., Selvaraj K., and Kao S.J. 2011. The fluvial geochemistry, contributions of silicate, carbonate and saline–alkaline components to chemical weathering flux and controlling parameters: Narmada River (Deccan Traps), India. Geochimica et Cosmochimica Acta, 75(3), pp.800-824.

Gwizd S., Fedo C., Grotzinger J., Edgett K., Rivera-Hernandez F., and Stein N. 2018. Depositional History of the Hartmann's Valley Member, Murray Formation, Gale Crater, Mars. In Lunar and Planetary Science Conference, The Woodlands, TX (Vol. 49, p. 2150).

Hagerty J.J., and Newsom H.E. 2003. Hydrothermal alteration at the Lonar Lake impact structure, India: Implications for impact cratering on Mars. Meteoritics & Planetary Science, 38(3), pp.365-381.

Harker R.I. 1959. The synthesis and stability of tilleyite, Ca5Si2O7(CO3)2. American Journal of Science, 257(9), 656-667.

Hausrath E.M., Ming D.W., Peretyazhko T. S., and Rampe E. B. 2018. Reactive transport and mass balance modeling of the Stimson sedimentary formation and altered fracture zones constrain diagenetic conditions at Gale crater, Mars.– Earth and Planetary Science Letter, 491, 1–10.

Heydari E., Parker T.J., Calef III F.J., Schroeder J.F., Van Beek J., Rowland S.K., and Fairen A.G. 2018. Characteristics and the Origin of the Vera Rubin Ridge, Gale Crater, Mars. In

Proceedings Lunar and Planetary Science Conference, The Woodlands, TX (Vol. 49, p. 1817).

Hicks L.J., Bridges J.C., and Gurman S.J. 2014. Ferric saponite and serpentine in the nakhlite martian meteorites. Geochimica et Cosmochimica Acta, 136, 194-210.

Holland T.J.B., and Powell R. 1998. An internally consistent thermodynamic data set for phases of petrological interest. J. Metamorph. Geol. 16, 309–343.

Horgan B.H.N., Johnson J.R., Fraeman A.A., Rice M.S., Seeger C., Bell III J.F., Bennett K.A., Cloutis E.A., Edgar L.A., Frydenvang J., Grotzinger J.P., L'Haridon J., Jacob S.R., Mangold N., Rampe E.B., Rivera-Hernandez F., Sun V.Z., Thompson L.M., and Wellington D. 2020. Diagenesis of Vera Rubin Ridge, Gale Crater, Mars from Mastcam Multispectral Images. Journal of Geophysical Research: Planets, 125, e2019JE006322.

Hurowitz J.A., Grotzinger J.P., Fischer W.W., McLennan S.M., Milliken R.E., Stein N., Vasavada A.R., Blake D.F., Dehouck E., Eigenbrode J.L., Fairén A.G., Frydenvang J., Gellert R., Grant J.A., Gupta S., Herkenhoff K.E., Ming D.W., Rampe E.B., Schmidt M.E., Siebach K.L., Stack-Morgan K., Sumner D.Y., and Wiens R.C. 2017. Redox stratification of an ancient lake in Gale Crater, Mars. Science, v. 356, no. 6341, p. eeah6849.

Jankowski B. 1977. Die Postimpakt-Sedimente in der Forschungsbohrung Nördlingen 1973. - Geologica Bavarica, 75: 21-36.

Kalleson E., Dypvik H., and Naterstad J. 2008. Postimpact sediments in the Gardnos impact structure, Norway. SPECIAL PAPERS-GEOLOGICAL SOCIETY OF AMERICA, 437, p.19.

Kühn M. 2004. Reactive flow modeling of hydrothermal systems. Lect. Notes Earth Sci. 103, 261 p.

L'Haridon J., Mangold N., Meslin P.Y., Johnson J.R., Rapin W., Forni O., Cousin A., Payré V., Dehouck E., Nachon M., Le Deit L., Gasnault O., Maurice S., and Wiens R.C. 2018. Chemical variability in mineralized veins observed by ChemCam on the lower slopes of Mount Sharp in Gale crater, Mars. Icarus, 311, 69-86.

L'Haridon J., Mangold N., Fraeman A.A., Johnson J.R., Cousin A., Rapin W., David G., Dehouck E., Sun V., Frydenvang J., Gasnault O., Gasda P., Lanza N., Forni O., Meslin P.-Y., Schwenzer S.P., Bridges J., Horgan B., House C.H., Salvatore M., Maurice S., and Wiens R.C. 2020. Iron Mobility During Diagenesis the Vera Rubin Ridge, Gale Crater, Mars. Journal of Geophysical research: Planets, 125, e2019JE006299.

Mangold N., Dehouck E., Fedo C., Forni O., Achilles C., Bristow T., Downs R.T., Frydenvang J., Gasnault O., L'Haridon J., Le Deit L., Maurice S., McLennan S.M., Meslin P.-Y., Morrison S., Newsom H.E., Rampe E., Rapin W., Rivera-Hernandez F., Salvatore M., and Wiens R.C. 2019a. Chemical alteration of fine-grained sedimentary rocks at Gale crater. Icarus, 321, 619-631.

Mangold N., Cousin A., Dehouck E., Forni O., Fraeman A., Frydenvang J., Gasnault O., Johnson J., Le Deit J.L., L'Haridon J., Le Mouélic S., Maurice S., McLennan S.M., Meslin P.-Y., Hewsom H.E., Rapin W., Rivera-Hernandez F., and Wiens R.C. 2019b. Chemostratigraphy of Fluvial and Lacustrine Sedimentary Rocks at Gale Crater Using

Chemcam Onboard the Curiosity Rover. Ninth International Conference on Mars. Abstract #6078.

Marion D. M., Catling D. C., and Karegel J. S. 2003. Modeling aqueous ferrous iron chemistry at low temperatures with application to Mars. Geochim. Cosmochim. Acta, 22, 4251–4266.

Martin P.E., Farley K.A., Baker M.B., Malespin C.A., Schwenzer S.P., Cohen B.A., Mahaffy P.R., McAdam A.C., Ming D.W., Vasconcelos P.M., and Navarro-González R. 2017. A two-step K-Ar experiment on Mars: Dating the diagenetic formation of jarosite from Amazonian groundwaters. Journal of Geophysical Research: Planets, 122(12), 2803-2818.

McAdam A.C., Sutter B., Douglas Archer P., Franz H.B., Wong G.M., Lewis J.M.T., Eigenbrode J.L., Stern J.C., Knudson C.A., Clark J.V., Andrejkovičová S., Ming D.W., Morris R.V., Achilles C.N., Rampe E.B., Bristow T.F., Navarro-González R., Mahaffy P.R., Thompson L.M., Gellert R., Williams A.J., House C.H., and Johnson S.S. 2020. Constraints on the Mineralogy and Geochemistry of the Vera Rubin Ridge, Gale Crater, Mars From Mars Science Laboratory Sample Analysis at Mars Evolved Gas Analysis. Journal of Geophysical Research: Planets, 125, 2019JE006309.

McAdam A. C., Zolotov M. Y., Mironenko M. V. and Sharp G. 2008. Formation of silica by low temperature acid alteration of Martian rocks: Physical-chemical constraints. Journal of Geophysical Research, **113**: doi10,1029/2007JE003056.

Melwani Daswani M., Schwenzer S.P., Reed M.H., Wright I.P., and Grady M.M. 2016. Alteration minerals, fluids, and gases on early Mars: Predictions from 1-D flow geochemical modeling of mineral assemblages in meteorite ALH 84001. Meteoritics & Planetary Science, 51(11), 2154-2174.

Meslin P.Y., Gasda P., L'Haridon J., Forni O., Lanza N., Lamm S., Johnson J.R., Wiens R.C., Thompson L., Rapin W., Gasnault O., Cousin A., Mangold N., Dehouck E., Maurice S., Lasue J., and Frydenvang J. 2018. Detection of Hydrous Manganese and Iron Oxides with Variable Phosphorus and Magnesium Contents in the Lacustrine Sediments of the Murray Formation, Gale, Mars. In Lunar and Planetary Science Conference (Vol. 49, p. 1447).

Milliken R.E., Grotzinger J.P., and Thomson B.J. 2010. Paleoclimate of Mars as captured by the stratigraphic record in Gale Crater. Geophysical Research Letters, v. 37, no. 4, p. L04201.

Minissale A., Vaselli O., Chandrasekharam D., Magro G., Tassi F., and Casiglia A. 2000. Origin and evolution of “intracratonic” thermal fluids from central-western peninsular India, Earth Planet. Sci. Lett., 181(3), 377–394.

Misra K.C. 2012. Introduction to geochemistry: principles and applications. John Wiley & Sons.

Morrison S.M., Downs R.T., Blake D.F., Vaniman D.T., Ming D.W., Hazen R.M., Treiman A.H., Achilles C.N., Yen A.S., Morris R.V., Rampe E.B., Bristow T.F., Chipera S.J., Sarrazin P.C., Gellert R., Fendrich K.V., Morookian J.M., Farmer J.D., Des Marais D.J., and Craig P.I. 2018. Crystal chemistry of martian minerals from Bradbury Landing through Naukluft Plateau, Gale crater, Mars. Am. Mineral. 103(6), 857-871.

Murchie S., Arvidson R., Bedini P., Beisser K., Bibring J.P., Bishop J., Boldt J., Cavender P., Choo T., Clancy R.T., Darlington E.H., Des Marais D., Espiritu R., Fort D., Green R., Guinness E., Hayes J., Hash C., Heffernan K., Hemmler J., Heyler G., Humm D., Hutcheson J., Izenberg N., Lee R., Lees J., Lohr D., Malaret E., Martin T., McGovern J.A., McGuire P., Morris R., Mustard J., Pelkey S., Rhodes E., Robinson M., Roush T., Schaefer E., Seagrave G., Seelos F., Silverglate P., Slavney S., Smith M., Shyong W.J., Strohbehn K., Taylor H., Thompson P., Tossman B., Wirzburger M., and Wolff M. 2007. Compact reconnaissance imaging spectrometer for Mars (CRISM) on Mars reconnaissance orbiter (MRO). Journal of Geophysical Research: Planets, 112(E5S03).

Muttik N., Kirsimaee K., Somelar P., and Osinski G.R. 2008. Post-impact alteration of surficial suevites in Ries crater, Germany: Hydrothermal modification or weathering processes?. Meteoritics & Planetary Science, 43(11), pp.1827-1840.

Nachon M., Clegg S.M., Mangold N., Schröder S., Kah L.C., Dromart G., Ollila A., Johnson J.R., Oehler D.Z., Bridges J.C., Le Mouélic S., Forni O., Wiens R.C., Anderson R.B., Blaney D.L., Bell III J.F., Clark B., Cousin A., Dyar M.D., Ehlmann B., Fabre C., Gasnault O., Grotzinger J., Lasue J., Lewin E., Léveillé R., McLennan S., Meslin P.-Y., Rapin W., Rice M., Squyres S.W., Stack K., Sumner D.Y., Vaniman D., and Wellington D. 2014. Calcium sulfate veins characterized by ChemCam/Curiosity at Gale crater, Mars. Journal of Geophysical Research: Planets, 119(9), 1991-2016.

Olsson-Francis K., Pearson V.K., Steer E.D., and Schwenzer S.P. 2017. Determination of Geochemical Bio-Signatures in Mars-Like Basaltic Environments. Frontiers in Microbiology, 8: article no. 1668.

Osinski G.R., Tornabene L.L., Banerjee N.R., Cockell C.S., Flemming R., Izawa M.R., McCutcheon J., Parnell J., Preston L.J., Pickersgill A.E., Pontefact A., Sapers H.M., and Southam G. 2013. Impact-generated hydrothermal systems on Earth and Mars. Icarus, 224(2), pp.347-363.

Palandri J.L. and Reed M.H. 2004. Geochemical models of metasomatism in ultramafic systems: serpentinization, rodingitization, and sea floor carbonate chimney precipitation. Geochimica et Cosmochimica Acta, 68(5), 1115-1133.

Peng Z.X., Mahoney J.J., Hooper P.R., Macdougall J.D., and Krishnamurthy P. 1998. Basalts of the northeastern Deccan Traps, India: isotopic and elemental geochemistry and relation to southwestern Deccan stratigraphy. Journal of Geophysical Research: Solid Earth, 103(B12), pp.29843-29865.

Peretyazhko T.S., Fox A., Sutter B., Niles P.B., Adams M., Morris R.V., and Ming D.W. 2016. Synthesis of akaganeite in the presence of sulfate: Implications for akaganeite formation in Yellowknife Bay, Gale Crater, Mars. Geochimica et Cosmochimica Acta, 188, 284-296.

Peretyazhko T.S., Ming D.W., Rampe E.B., Morris R.V., and Agresti D.G. 2018. Effect of solution pH and chloride concentration on akaganeite precipitation: Implications for akaganeite formation on Mars. Journal of Geophysical Research: Planets, 123(8), 2211-2222.

Pinckney L.R. and Burnham C.W. 1988. Effects of compositional variation on the crystal structures of pyroxmangite and rhodonite. American Mineralogist, 73(7-8), 798-808.

Rampe E.B., Ming D.W., Blake D.F., Bristow T.F., Chipera S.J., Grotzinger J.P., Morris R.V., Morrison S.M., Vaniman D.T., Yen A.S., Achilles C.N., Craig P.I., Des Marais D.J., Downs R.T., Farmer J.D., Fendrich K.V., Gellert R., Hazen R.M., Kah L.C., Morookian J.M., Peretyazhko T.S., Sarrazin P., Treiman A.H., Berger J.A., Eigenbrode J., Fairén A.G., Forni O., Gupta S., Hurowitz J.A., Lanza N.L., Schmidt M.E., Siebach K., Sutter B., and Thompson L.M. 2017. Mineralogy of an ancient lacustrine mudstone succession from the Murray formation, Gale crater, Mars. Earth and Planetary Science Letters, 471, 172-185.

Rampe E.B., Blake D.F., Bristow T.F., Ming D.W., Vaniman D.T., Morris R.V., Achilles C.N., Chipera S.J., Morrison S.M., Tu V.M., Yen A.S., Castle N., Downs G.W., Downs R.T., Grotzinger J.P., Hazen R.M., Treiman A.H., Peretyazhko T.S., Des Marais D.J., Walroth R.C., Craig P.I., Crisp J.C., Lafuente B., Morookian J.M., Sarrazin P.C., Thorpe M.T., Bridges J.C., Edgar L.A., Fedo C.M., Freissinet C., Gellert R., Mahaffy P.R., Newsom H.E., Johnson J.R., Kah L.C., Siebach K.L., Schieber J., Sun V.Z., Vasavada A.R., Wellington D., Wiens R.C., and the MSL Science Team 2020a. Mineralogy and Geochemistry of Sedimentary Rocks and Eolian Sediments in Gale Crater, Mars: A Review after Six Earth Years of Exploration with *Curiosity*. Geochemistry, 80(2), 125605, doi: 10.1016/j.chemer.2020.125605.

Rampe E.B., Bristow T.F., Morris R.V., Morrison S.M., Achilles C.N., Ming D.W., Vaniman D.T., Blake D.F., Tu V.M., Chipera S.J., Yen A.S., Peretyazhko T.S., Downs R.T., Hazen R.M., Treiman A.H., Grotzinger J.P., Castle N., Craig P.I., Des Marais D.J., Thorpe M.T., Walroth R.C., Downs G.W., Fraeman A.A., Siebach K.L., Gellert R., Lafuente B., McAdam A.C., Meslin P.-Y., Sutter B., and Salvatore M.R. 2020b. Mineralogy of Vera Rubin ridge from the Mars Science Laboratory CheMin instrument. Journal of Geophysical Research: Planets, 125, e2019E006306.

Rapin W., Ehlmann B.L., Dromart G., Schieber J., Thomas N.H., Fischer W.W., Fox V.K., Stein N.T., Nachon M., Clark B.C., Kah L.C., Thompson L., Meyer H.A., Gabriel T.S.J., Hardgrove C., Mangold N, Rivera-Hernandez F., Wiens R.C., and Vasavada A.R. 2019. An interval of high salinity in ancient Gale crater lake on Mars. Nature Geoscience, 12, 889-895.

Reed M.H. 1983. Seawater-basalt reaction and the origin of greenstones and related ore deposits. Economic Geology, 78(3), 466-485.

Reed M.H. 1997. Hydrothermal alteration and its relationship to ore fluid composition. In: Barnes, H.L. (Ed.), Geochemistry of Hydrothermal Ore Deposits, third ed. John Wiley & Sons, New York, pp. 303–365.

Reed M.H., Spycher N.F., and Palandri J. 2010. User Guide for CHIM-XPT: A Program for Computing Reaction Processes in Aqueous-Mineral-Gas Systems and MINTAB Guide. 71p., University of Oregon, Eugene.

Rimstidt J.D. 2014. Geochemical Rate Models. An Introduction to Geochemical Kinetics. Cambridge University Press, New York, 232p.

Rivera-Hernandez F., Sumner D.Y., Mangold N., Stack K.M., Edgett K.S., Bennett K.A., Wiens R.C., Sun V.Z., Heydari E., and Maurice S. 2019. Vera Rubin Ridge (Gale Crater, Mars)

Grain Size Observations from ChemCam LIBS Data, and Interpretations. In Proceedings Lunar and Planetary Science Conference, The Woodlands, TX (Vol. 50, p. 3029).

Robinson D., and Bevins R.E. 1999. Patterns of regional low-grade metamorphism in metabasites, in Low-Grade Metamorphism, edited by M. Frey and D. Robinson, pp. 143–168, Blackwell Sci, Oxford, U.K.

Salil M.S., Shrivastava J.P., and Pattanayak S.K. 1997. Similarities in the mineralogical and geochemical attributes of detrital clays of Maastrichtian Lameta Beds and weathered Deccan basalt, Central India. Chemical Geology, 136(1-2), pp.25-32.

Schieber J., Bish D., Coleman M., Reed M., Hausrath E.M., Cosgrove J., Gupta S., Minitti M.E., Edgett K.S., and Malin M. 2017. Encounters with an unearthly mudstone: Understanding the first mudstone found on Mars. Sedimentology, 64, 311-358. doi:10.1111/sed.12318.

Schmieder M., Kennedy T., Jourdan F., Buchner E., and Reimold W.U. 2018. A high-precision 40Ar/39Ar age for the Nördlinger Ries impact crater, Germany, and implications for the accurate dating of terrestrial impact events. Geochimica et Cosmochimica Acta, 220, pp.146-157.

Schwenzer S.P. and Kring D.A. 2009. Impact-generated hydrothermal systems capable of forming phyllosilicates on Noachian Mars. Geology, 37(12), 1091-1094.

Schwenzer S.P. and Kring D.A. 2013. Alteration minerals in impact-generated hydrothermal systems – Exploring host rock variability Icarus, 226, 487-496.

Schwenzer S.P., Abramov O., Allen C.C., Bridges J.C., Clifford S.M., Filiberto J., Kring D.A., Lasue J., McGovern P.J., Newsom H.E., Treiman A.H., Vaniman D.T., Wiens R.C., and Wittmann A. 2012. Gale Crater: Formation and post-impact hydrous environments. Planetary and Space Science, 70(1), 84-95.

Schwenzer S.P., Bridges J.C., Wiens R.C., Conrad P.G., Kelley S.P., Leveille R., Mangold N., Martin-Torres J., McAdam A., Newsom H., Zorzano M.P., Rapin W., Spray J., Treiman A.H., Westall F., Fairén A.G., and Meslin P.-Y. 2016. Fluids during diagenesis and sulfate vein formation in sediments at Gale crater, Mars. Meteoritics & Planetary Science, 51(11), 2175-2202. doi: 10.1111/maps.12668.

Schwertmann U. and Murad E. 1983. Effect of pH on the formation of goethite and hematite from ferrihydrite. Clays and Clay Minerals, 31(4), pp.277-284.

Smith R.J., Dehouck E., and McLennan S. 2019. Amorphous Component Compositional Ranges in Gale Crater, Mars. Ninth International Conference on Mars, abstract #6324.

Stack K.M., Grotzinger J.P., Lamb M.P., Gupta S., Rubin D.M., Kah L.C., Edgar L.A., Fey D.A., Hurowitz J.A., McBride M., Rivera-Hernandez F., Sumner D.Y., van Beek J.K., Williams R.M.E., and Yingst R.A. 2019. Evidence for plunging river plume deposits in the Pahrump Hills member of the Murray formation, Gale crater, Mars. Sedimentology, 66(5), 1768-1802.

Stein N., Grotzinger J.P., Schieber J., Mangold N., Hallet B., Newsom H., Stack K.M., Berger J.A., Thompson L., Siebach K.L., Cousin A., Le Mouélic S., Minitti M., Sumner D.Y., Fedo C., House C.H., Gupta S., Vasavada A.R., Gellert R., Wiens R.C., Frydenvang J., Forni O., Meslin P.Y., Payré V., and Dehouck E. 2018. Desiccation cracks provide

evidence of lake drying on Mars, Sutton Island member, Murray formation, Gale Crater. Geology, 46(6), 515-518.

Sutter B., Mcadam A.C., Mahaffy P.R., Ming D.W., Edgett K.S., Rampe E.B., Eigenbrode J.L., Franz H.B., Freissinet C., Grotzinger J.P., Steele A., House C.H., Archer P.D., Malespin C.A., Navarro-González R., Stern J.C., Bell J.F., Calef F.J., Gellert R., Glavin D.P., Thompson L.M., and Yen A.S. 2017. Evolved gas analyses of sedimentary rocks and eolian sediment in Gale Crater, Mars: Results of the Curiosity rover's sample analysis at Mars instrument from Yellowknife Bay to the Namib Dune. Journal of Geophysical Research: Planets, 122(12), 2574-2609.

Tantawy M.A., Shatat M.R., El-Roudi A.M., Taher M.A., and Abd-El-Hamed M. 2014. Low temperature synthesis of belite cement based on silica fume and lime. International scholarly research notices, 2014.

Thompson L.M., Berger J.A., Spray J.G., Fraeman A.A., McCraig M.A., O'Connell-Cooper C.D., Schmidt M.E., VanBommel S., Gellert R., Yen A., and Boyd N.I. 2020. APXS-Derived Compositional Characteristics of Vera Rubin Ridge and Murray Formation, Gale Crater, Mars: Geochemical Implications for the Origin of the Ridge. Journal of Geophysical Research: Planets, 125, e2019JE006319.

Tosca N.J., McLennan S.M., Dyar M.D., Sklute E.C., and Michel F.M. 2008. Fe oxidation processes at Meridiani Planum and implications for secondary Fe mineralogy on Mars. Journal of Geophysical Research, **113**: doi: 10.1029/2007JE003019.

Tosca N.J., McLennan S.M., Lindsley D.H., and Schoonen M.H. 2004. Acid-sulfate weathering of synthetic Martian basalt: The acid fog model revisited. Journal of Geophysical Research, **109**: E 05003, doi: 10.1029/2003JE002218, 29 p.

Treiman A.H., and Essene E.J. 1983. Phase equilibria in the system CaO-SiO2-CO2. American Journal of Science A, 283, 97-120.

Treiman A.H., Morris R.V., Agresti D.G., Graff T.G., Achilles C.N., Rampe E.B., Bristow T.F., Ming D.W., Blake D.F., Vaniman D.T., Bish D.L., Chipera S.J., Morrison S.M., and Downs R.T. 2014. Ferrian saponite from the Santa Monica Mountains (California, USA, Earth): Characterization as an analog for clay minerals on Mars with application to Yellowknife Bay in Gale Crater. American Mineralogist, 99(11-12), 2234-2250, http://dx.doi.org/10.2138/am-2014-4763.

Turner S.M.R., Schwenzer S.P., Bridges J.C., Bedford C.C., Rampe E.B., Fraeman A.A., McAdam A., Mangold N., and L'Haridon J. 2019. Thermochemical Modelling of Fluid-Rock Reactions in Vera Rubin ridge, Gale crater, Mars. In Lunar and Planetary Science Conference (Vol. 50, p. 1897).

Vaniman D.T., Bish D.L., Ming D.W., Bristow T.F., Morris R.V., Blake D.F., Chipera S.J., Morrison S.M., Treiman A.H., Rampe E.B., Rice M., Achilles C.N., Grotzinger J.P., McLennan M., Williams J., Bell III J.F., Newsom H.E., Downs R.T., Maurice S., Sarrazin P., Yen A.S., Morookian J.M., Farmer J.D., Stack K., Milliken R.E., Ehlmann B.L., Sumner D.Y., Berger G., Crisp J.A., Hurowitz J.A., Anderson R., Des Marais D.J., Stolper E.M., Edgett K.S., Gupta S., Spanovich N., and the MSL Science Team 2014. Mineralogy of a mudstone at Yellowknife Bay, Gale crater, Mars. Science, 343(6169), p.1243480.

Varnes E.S., Jakorsky B.M., and McCollom T.M. 2003. Biological Potential of martian Hydrothermal Systems. Astrobiology, **3**: 407–414.

Vernié P., Kienast J.R. and Mével C. 1986. The occurrence of deerite in highly oxidizing conditions within the 'schistes lustrés' of eastern Corsica. Journal of Metamorphic Geology, 4(4), 385-399.

von Engelhardt W. 1997. Suevite breccia of the Ries impact crater, Germany: Petrography, chemistry and shock metamorphism of crystalline rock clasts. Meteoritics & Planetary Science, 32(4), pp.545-554.

Williams R.M.E., Grotzinger J.P., Dietrich W.E., Gupta S., Sumner D.Y., Wiens R.C., Mangold N., Malin M.C., Edgett K.S., Maurice S., Forni O., Gasnault O., Ollila A., Newsom H.E., Dromart G., Palucis M.C., Yingst R.A., Anderson R.B., Herkenhoff K.E., Le Mouélic S., Goetz W., Madsen M.B., Koefoed A., Jensen J.K., Bridges J.C., Schwenzer S.P., Lewis K.W., Stack K.M., Rubin D., Kah L.C., Bell III J.F., Farmer J.D., Sullivan R., Van Beek T., Blaney D.L., Pariser O., Deen R.G., and the MSL Science Team 2013. Martian fluvial conglomerates at Gale crater. science, 340(6136), pp.1068-1072.

Wong G.M., Lewis J.M.T., Knudson C.A., Millan M., McAdam A.C., Eigenbrode J.L., Andrejkovičová S., Gómez F., Navarro-González R., and House C.H. 2020. Detection of Reduced Sulfur on Vera Rubin Ridge by Quadratic Discriminant Analysis of Volatiles Observed During Evolved Gas Analysis. Journal of Geophysical Research: Planets, 125, e2019JE006304.

Zolotov M.Y. and Mironenko M.V. 2007. Timing of acid weathering on mars: A kinetic-thermodynamic assessment. Journal of Geophysical Research, **112**: doi: 10.1029/2006JE002882, 20p.

Zolotov M.Y. and Mironenko M.V. 2016. Chemical models for martian weathering profiles: Insights into formation of layered phyllosilicate and sulfate deposits. Icarus, 275. 203-220.

Zolotov M.Y. and Shock E.L. 1999. Abiotic synthesis of polycyclic aromatic hydrocarbons on Mars. Journal of Geophysical Research, **104**: 14033–14049.

Zolotov M.Y. and Shock E.L. 2005. Formation of jarosite-bearing deposits through aqueous oxidation of pyrite at Meridani Planum, Mars. Geophysical Research Letters, **32**: doi: 10.1029/2005GL024253, 5 p.

Figures and Tables

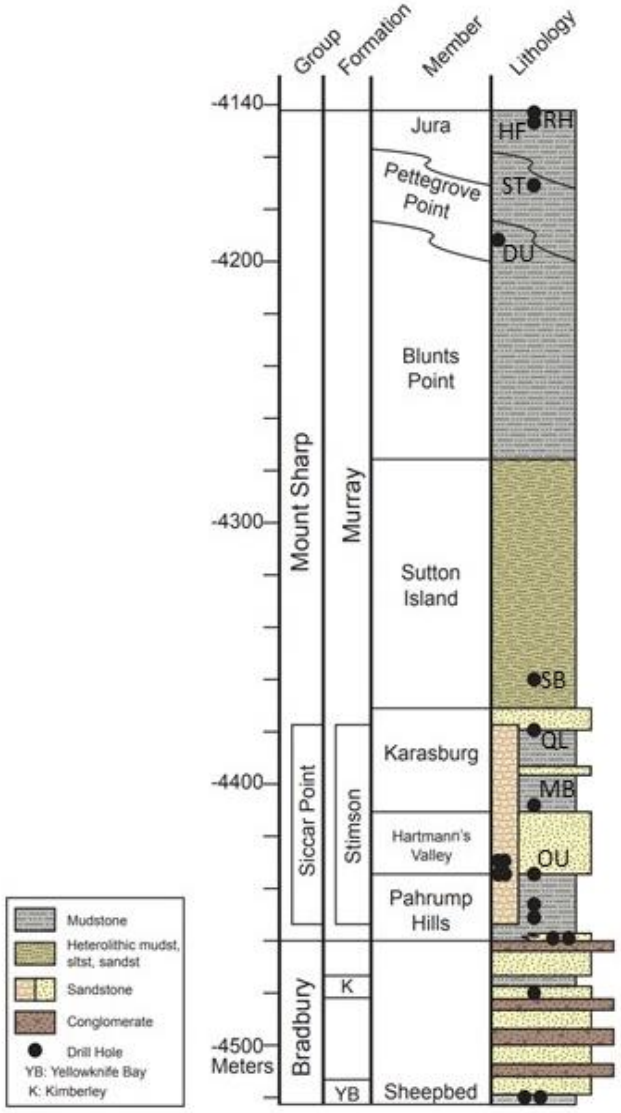

Figure 1: Stratigraphic column detailing the morphological characteristics of the stratigraphic groups and units encountered by the *Curiosity* rover up to and including the Jura member. Drill holes of interest in this study are annotated: Oudam (OU), Marimba (MB), Quela (QL), Sebina (SB), Duluth (DU), Stoer (ST), Highfield (HF), and Rock Hall (RH). Image credit: The MSL sedimentology and stratigraphy working group.

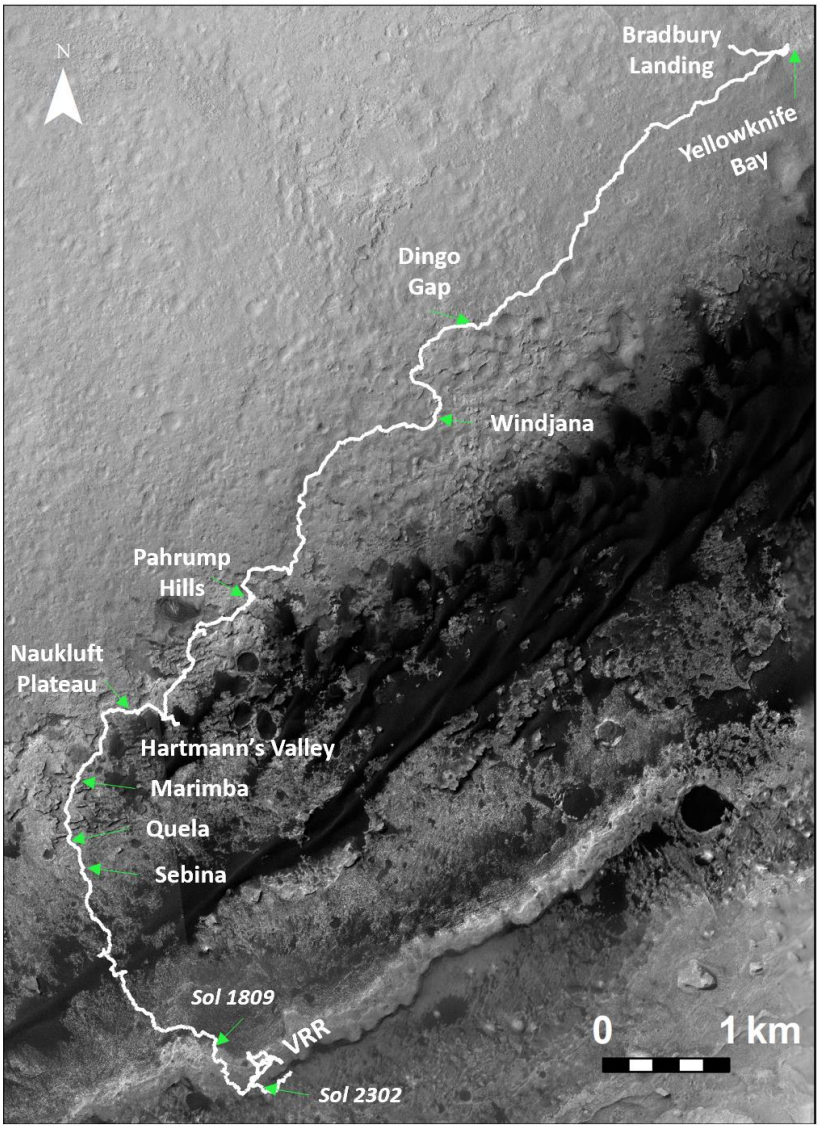

Figure 2: HiRISE orbital overview of the NASA Mars Science Laboratory *Curiosity* rover's traverse from Bradbury Landing up to sol 2359. Select locations are annotated as well as sol 1809 when *Curiosity* ascended on to Vera Rubin ridge (VRR), and sol 2302 when *Curiosity* traversed off VRR and into the Clay Bearing Unit. Adapted image from NASA-JPL/Fraeman.

Table 1: Ratio of alteration to primary mineral content per drill hole, including and excluding amorphous component as an alteration component. Ca-sulfates were excluded. Errors propagated from uncertainty in CheMin mineral abundances. Pyroxenes and feldspars were considered to be primary minerals. Fe-oxides, jarosite, quartz, halite, fluorapatite and phyllosilicates were considered to be alteration. Source data take from Achilles et al. (2020) and Rampe et al. (2020b).

Drill hole	Including Amorphous	Excluding Amorphous
Oudam	2.1 ± 0.4	0.6 ± 0.1
Marimba	4.9 ± 0.8	2.3 ± 0.3
Quela	4.1 ± 0.8	1.3 ± 0.1
Sebina	5.3 ± 1.0	1.8 ± 0.2
Duluth	2.9 ± 0.3	0.8 ± 0.3
Stoer	2.3 ± 0.2	1.0 ± 0.2
Highfield	2.5 ± 0.2	0.6 ± 0.1
Rock Hall	2.0 ± 0.6	0.9 ± 0.2

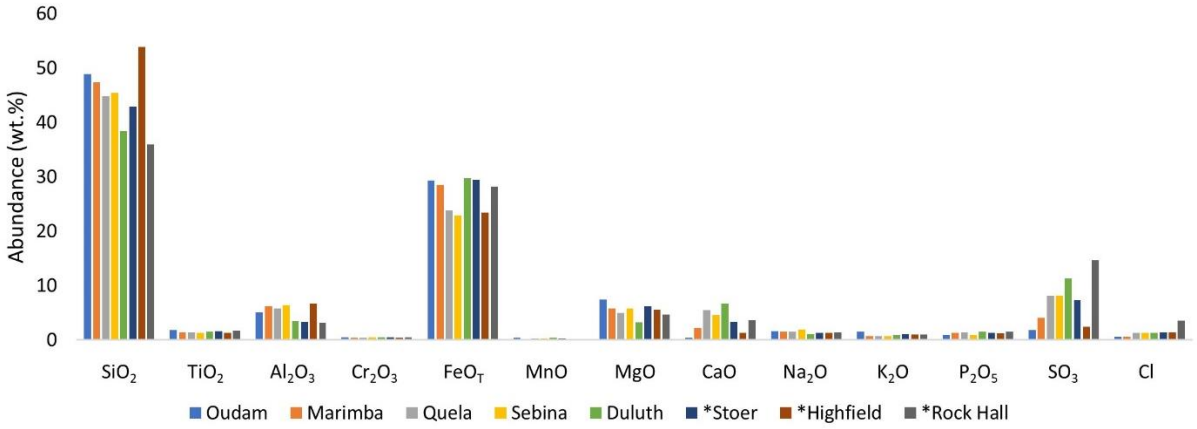

Figure 3: Main-phase alteration assemblage compositions for Oudam, Marimba, Quela, Sebina, Duluth, Stoer, Highfield and Rock Hall. Calculated using APXS and CheMin results (Achilles et al., 2020; Rampe et al., 2020b), as explained in methods section 2.2. Samples Oudam, Marimba, Quela, Sebina, and Duluth are from pre-VRR Murray formation localities. Stoer, Highfield and Rock Hall represent VRR Murray. *indicates drill samples acquired form VRR.

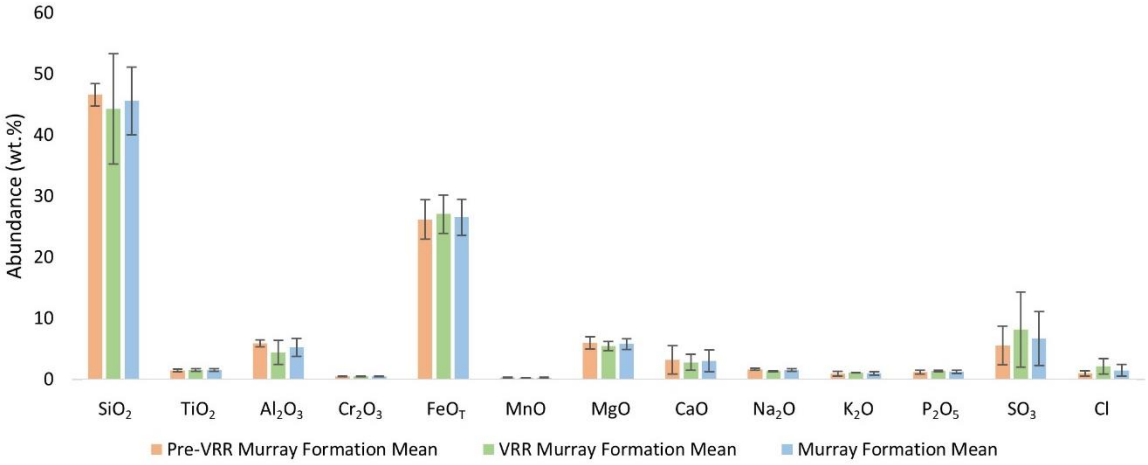

Figure 4: Mean alteration compositions for the Pre-VRR Murray formation (Oudam, Marimba, Quela, Sebina), VRR Murray Formation (Stoer, Highfield and Rock Hall), the overall Murray Formation. Calculated using APXS and CheMin results. Error bars show standard deviation for each calculated mean, illustrating the statistical similarity between the calculated alteration compositions.

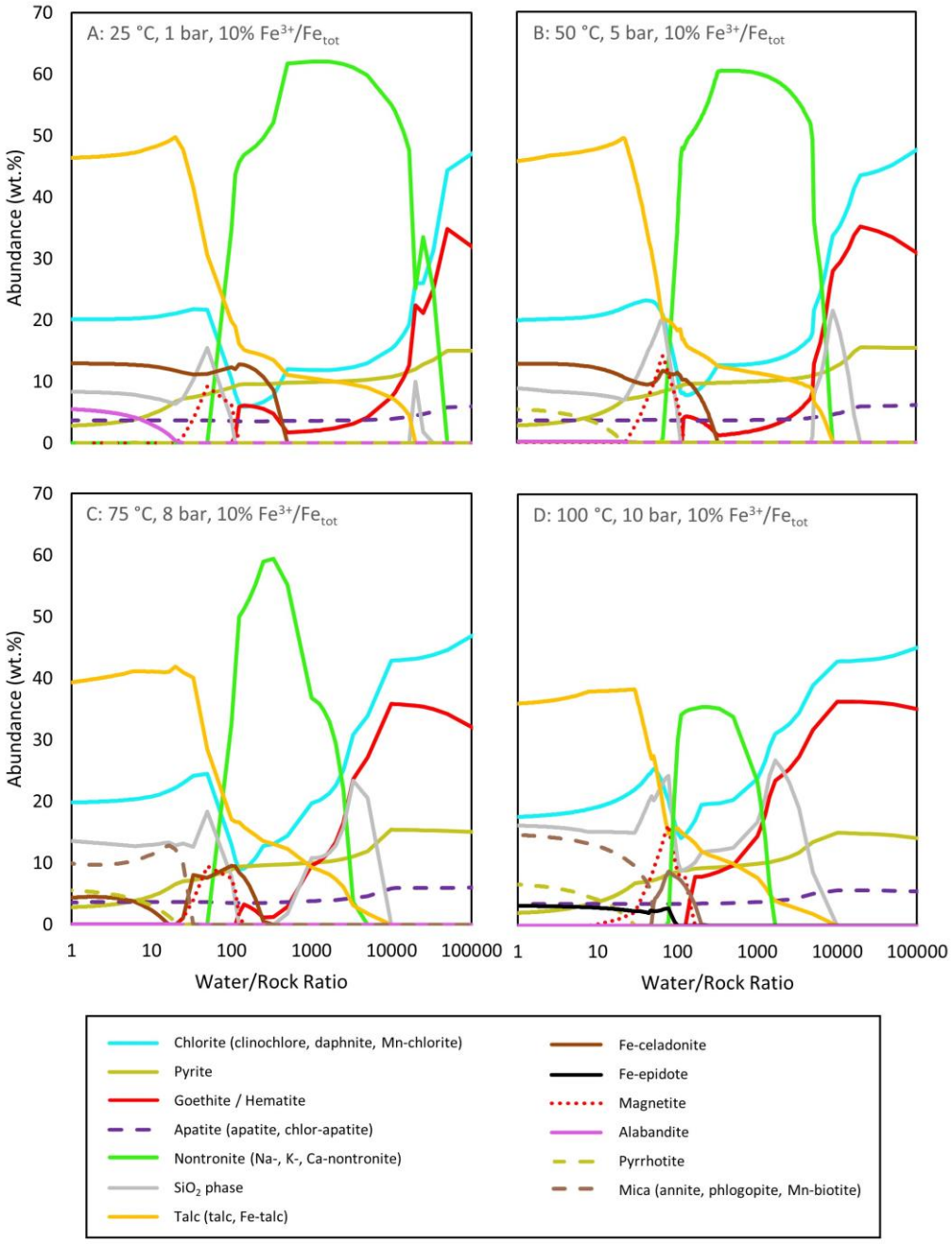

Figure 5: CHIM-XPT results for the calculated VRR alteration composition (Table S4) reacted with GPW (Bridges et al., 2015b). Reactions at 25, 50, 75 and 100 °C, and 10% of the FeO_T is Fe^{3+}, as indicated. Goethite only precipitated at 25 °C (A), and hematite did not precipitate at that temperature. K-nontronite precipitated at 25 °C (A), whereas Na-nontronite did not precipitate at 100 °C (D) and Ca-nontronite precipitated at all temperatures. Chlor-apatite formed at 25 °C (A), 50 °C (B) and 75 °C (C), whereas apatite formed at 75 °C (C) and 100 °C (D). Trace abundances of calcite, spurrite and merwinite are not included on the plots.

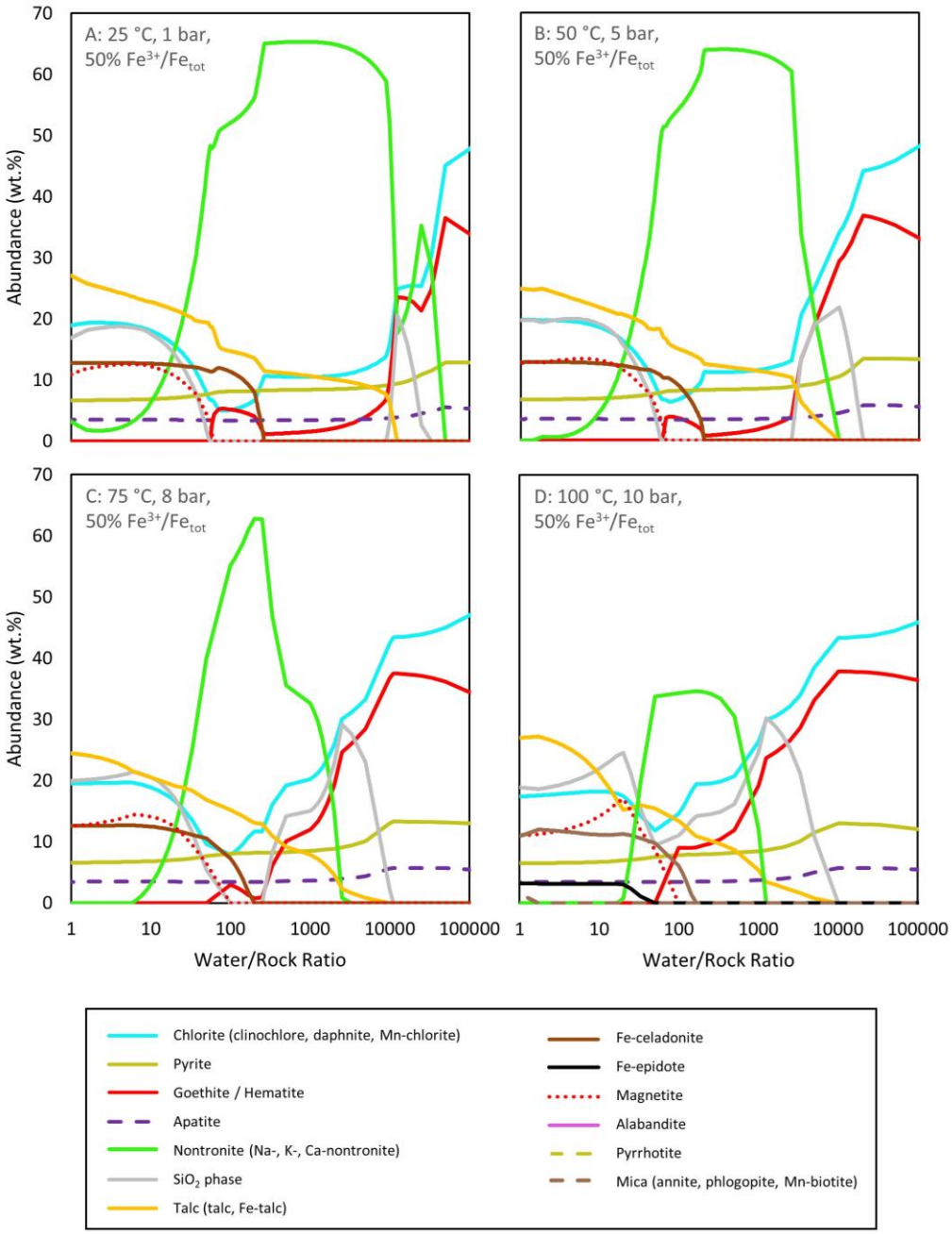

Figure 6: CHIM-XPT results for the calculated VRR alteration composition (Table S4) reacted with GPW (Bridges et al., 2015b). Reactions at 25, 50, 75 and 100 °C, and 50% of the FeO_T is Fe^{3+}, as indicated. Goethite only precipitated at 25 °C (A), and hematite did not precipitate at that temperature. K-nontronite precipitated at 25 °C (A) and 50°C (B), whereas Na-nontronite did not precipitate at 100 °C (D) and Ca-nontronite precipitated at all temperatures. Rhodochrosite precipitated at 25 °C (A) and 50 °C (B), and trace wt.% of calcite precipitated at all temperatures for 50% Fe^{3+}/Fe_{tot} (A,B,C,D). Trace abundances of calcite, rhodochrosite, spurrite and merwinite are not included on the plots.

Table 2: Summed VRR clay mineral wt.% / Fe-oxide wt.% ratio .% at high (10,000), intermediate (1,000) and low (100) W/R ratios in thermochemical models (Figures 6 and 7) using the calculated VRR mean alteration composition (Table S4) as the host rock (at both 10 and 50% Fe^{3+}/Fe_{tot}) reacted with GPW (Bridges et al., 2015b) at 25, 50, 75 and 100 °C using CHIM-XPT (Reed et al., 2010).

	10% Fe^{3+}/Fe_{tot} Models			50% Fe^{3+}/Fe_{tot} Models		
	10,000 W/R	1,000 W/R	100 W/R	10,000 W/R	1,000 W/R	100 W/R
25 °C	10.4	43.2	--	7.7	55.7	13.9
50 °C	1.2	40.7	--	1.2	46.0	21.4
75 °C	1.2	6.9	--	1.2	5.1	26.3
100 °C	1.2	3.8	--	1.1	2.3	6.9

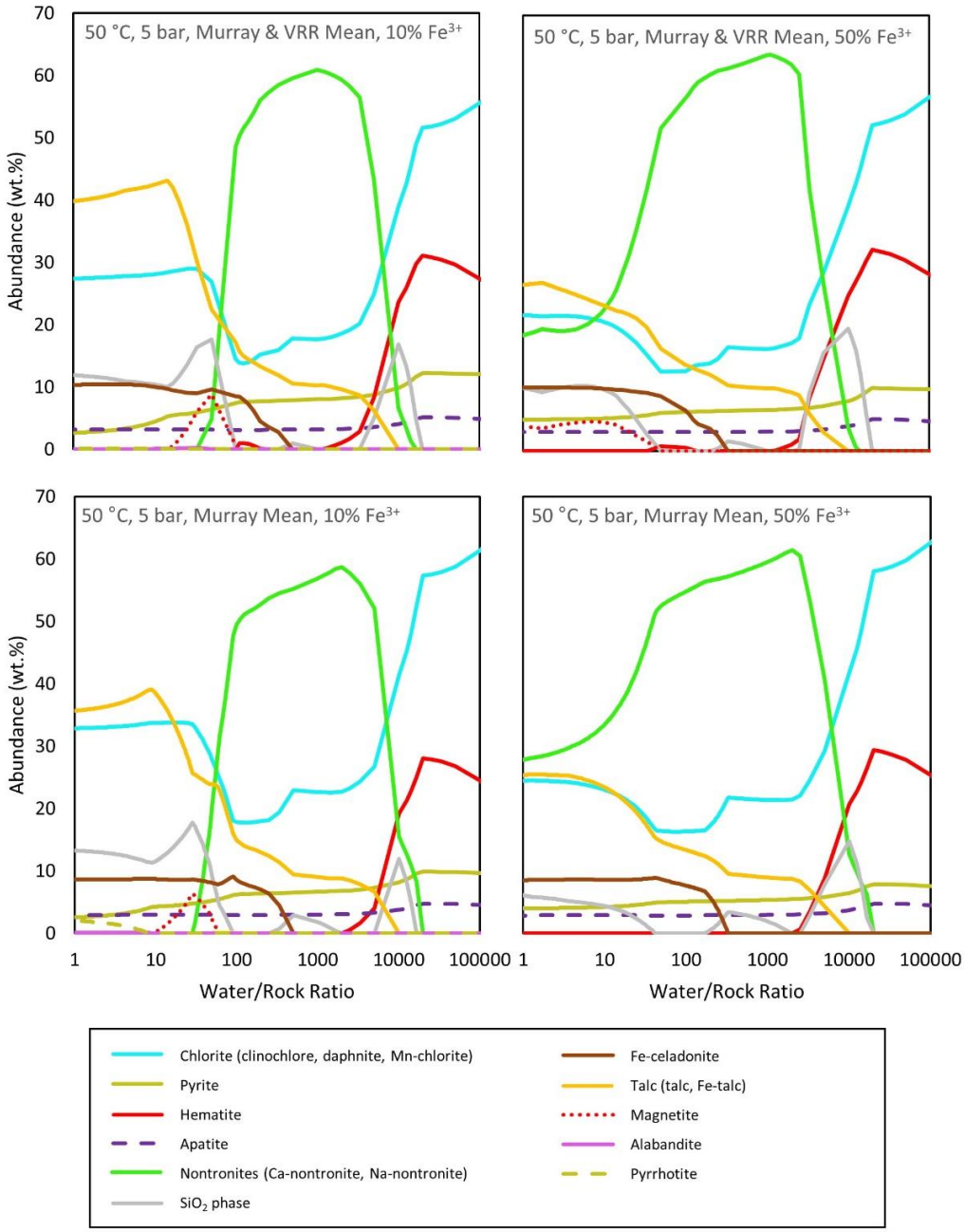

Figure 7: CHIM-XPT results for the calculated alteration composition for the Murray formation and the Murray and VRR (overall) (Table S4) reacted with GPW (Bridges et al., 2015b). Reactions are at 50 °C and the Fe^{3+} content of FeO_T is at 10 % and 50 %, as indicated. Trace abundances of rhodochrosite, calcite, spurrite and merwinite are not included on the plot.

Table 3: Summed clay wt.% / Fe-oxide wt.% ratio at high (10,000), intermediate (1,000) and low (100) W/R ratios in models for the pre-VRR Murray mean and overall mean calculated alteration compositions (Table S4) as the host rock, at 10 and 50% Fe^{3+}/Fe_{tot}, reacted with GPW (Bridges et al., 2015b) at 50 °C using CHIM-XPT (Reed et al., 2010).

	10% Fe^{3+}/Fe_{tot} Models			50% Fe^{3+}/Fe_{tot} Models		
	10,000 W/R	1,000 W/R	100 W/R	10,000 W/R	1,000 W/R	100 W/R
Pre-VRR	3.0	--	--	2.6	--	--
Overall	1.9	--	--	1.7	--	--

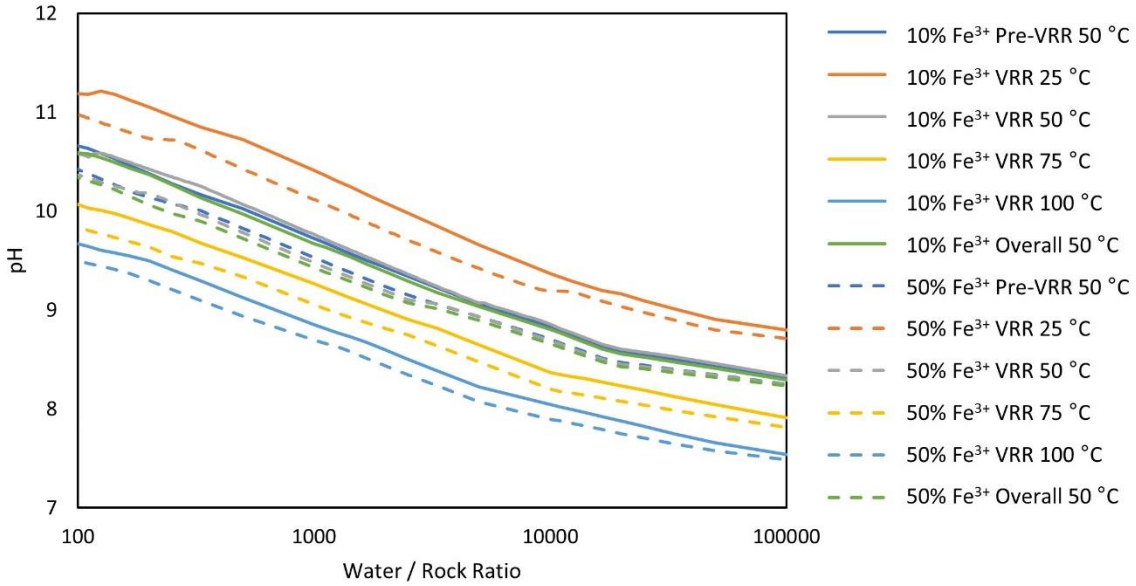

Figure 8: Plot showing pH variation with W/R for the CHIM-XPT models shown in Figures 5, 6 and 7. Starting compositions for Pre-VRR Murray, VRR Murray and Overall Murray used in the modeling are shown in Table S4.

Table 4: Calculated clay mineral / hematite and clay mineral / Fe-oxide sum for drilled samples in the pre-VRR Murray formation and VRR, determined using CheMin wt.% mineral abundances (Achilles et al., 2020; Rampe et al., 2020b). Means are included for pre-VRR and VRR samples, as well as an overall mean. Errors shown are propagated errors calculated from errors in mineral abundances.

Drill Hole	Clay mineral / Hematite	Clay mineral / Fe-oxide sum
Oudam	0.3 ± 0.1	0.3 ± 0.1
Marimba	4.4 ± 0.9	4.4 ± 0.9
Quela	2.3 ± 0.4	2.3 ± 0.4
Sebina	2.8 ± 0.6	2.8 ± 0.6
Duluth	2.4 ± 1.1	2.1 ± 1.0
Pre-VRR mean	*2.4 ± 0.3*	*2.4 ± 0.3*
Stoer	0.6 ± 0.3	0.6 ± 0.3
Highfield	0.5 ± 0.2	0.5 ± 0.2
Rock Hall	4.5 ± 2.1	1.5 ± 0.7
VRR mean	*1.9 ± 0.7*	*0.8 ± 0.3*
Overall mean	*2.2 ± 0.3*	*1.8 ± 0.2*

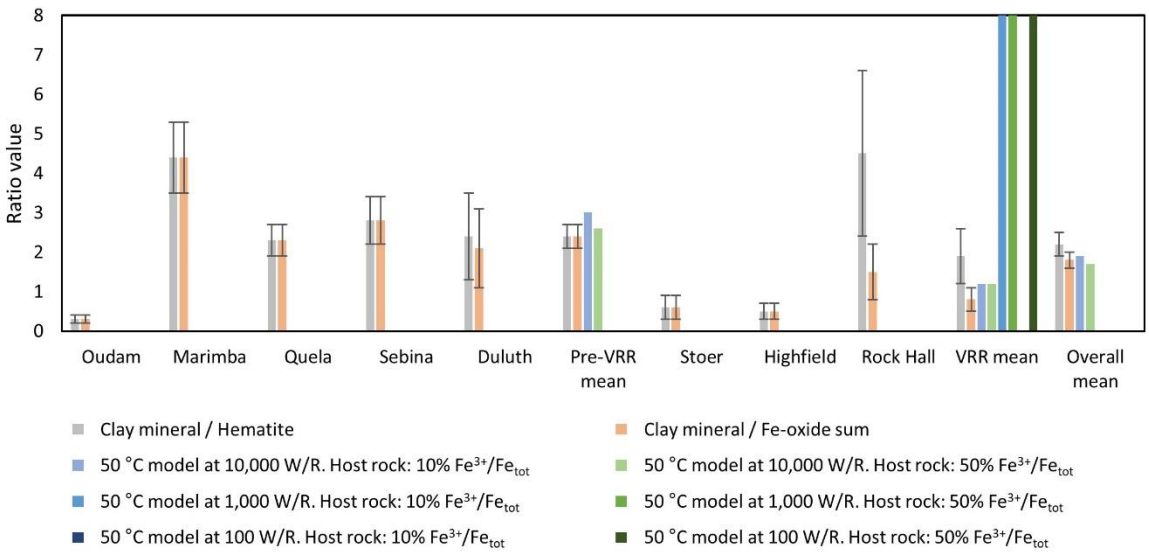

Figure 9: Plot comparing calculated clay mineral / hematite and clay mineral / Fe-oxide sum for drill samples in the pre-VRR Murray formation and VRR, determined using CheMin wt.% mineral abundances (Achilles et al., 2020; Rampe et al., 2020b). Means are included for pre-VRR and VRR samples, as well as an overall mean. Errors shown are propagated errors calculated from errors in mineral abundances. Values for models run at 50 °C at 10,000 W/R, 1,000 W/R and 100 W/R from Tables 2 and 3 are included for comparison.

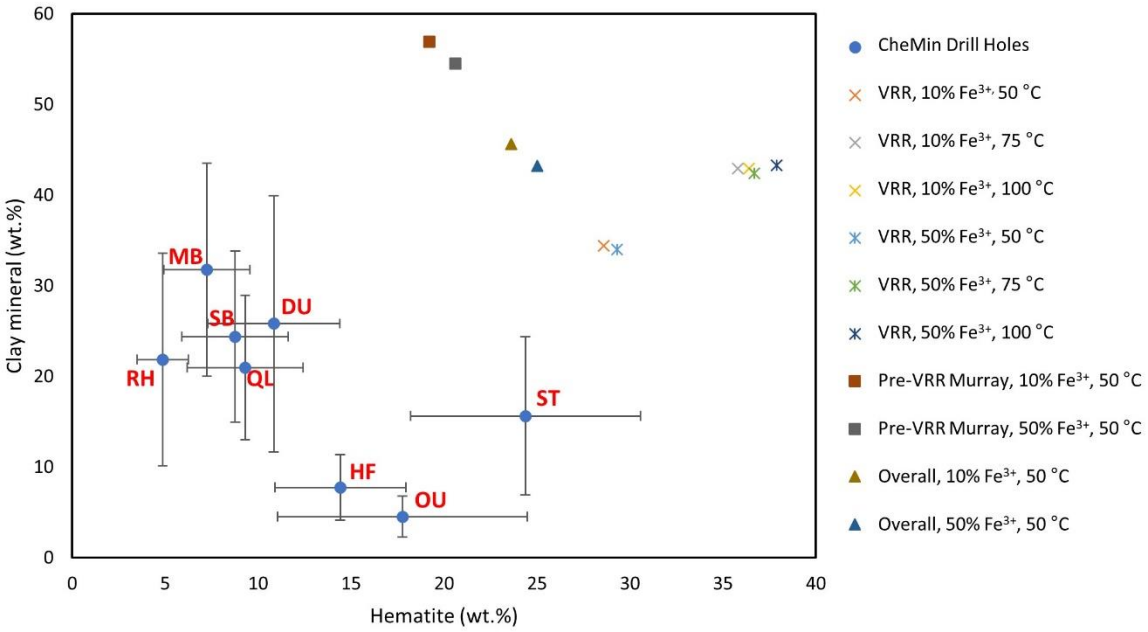

Figure 10: Clay mineral abundance vs hematite abundance from CheMin (Achilles et al., 2020; Rampe et al., 2020b) normalized to the alteration component (including amorphous phase) compared to CHIM-XPT results in this study (Figures 5, 6 and 7; Tables S5 and S8) at high (10,000) W/R. Drill holes Oudam, Marimba, Quela, Sebina, Duluth, Stoer, Highfield and Rock Hall are annotated with OU, MB, QL, SB, DU, ST, HF and RH, respectively. Linear regression carried out on thermochemical models at 50 °C in the figure revealed the trend $y = (-2.35 \pm 0.09)x + (102.15 \pm 2.16)$ with an R^2 value of 0.99. Comparative linear regression carried out on CheMin drill samples Oudam, Marimba, Sebina, Quela, Duluth, Highfield and Rock Hall in the figure gave a trend of $y = (-1.88 \pm 0.56)x + (39.23 \pm 6.24)$ with an R^2 value of 0.70. This trend changed to $y = (-2.56 \pm 0.45)x + (48.38 \pm 5.33)$ with an R^2 value of 0.89 with Rock Hall removed from the analysis.

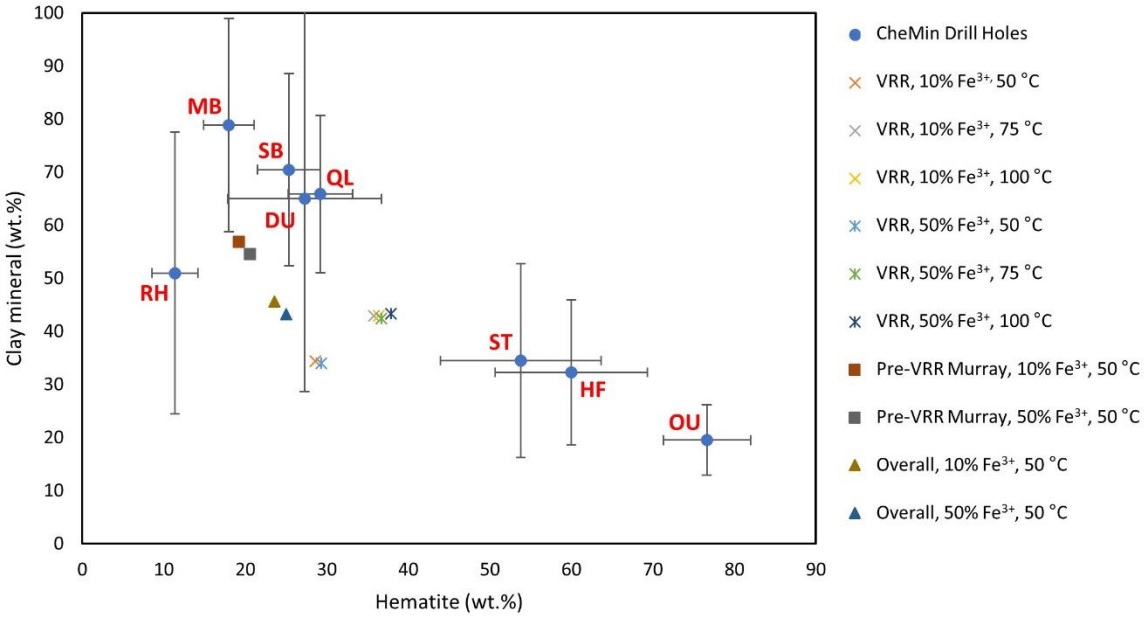

Figure 11: Clay mineral abundance vs hematite abundance from CheMin (Achilles et al., 2020; Rampe et al., 2020b) normalized to the alteration component (excluding the amorphous component) compared to CHIM-XPT results in this study (Figures 5, 6 and 7; Tables S5 and S8) at high (10,000) W/R. The comparable negative correlations of different gradients for the CheMin drill holes and the thermochemical models and the trend with temperature shown in Figure 10 indicates that only a part of the derived alteration composition is reactive. Drill hole names and abbreviations detailed in Figure 10 caption.

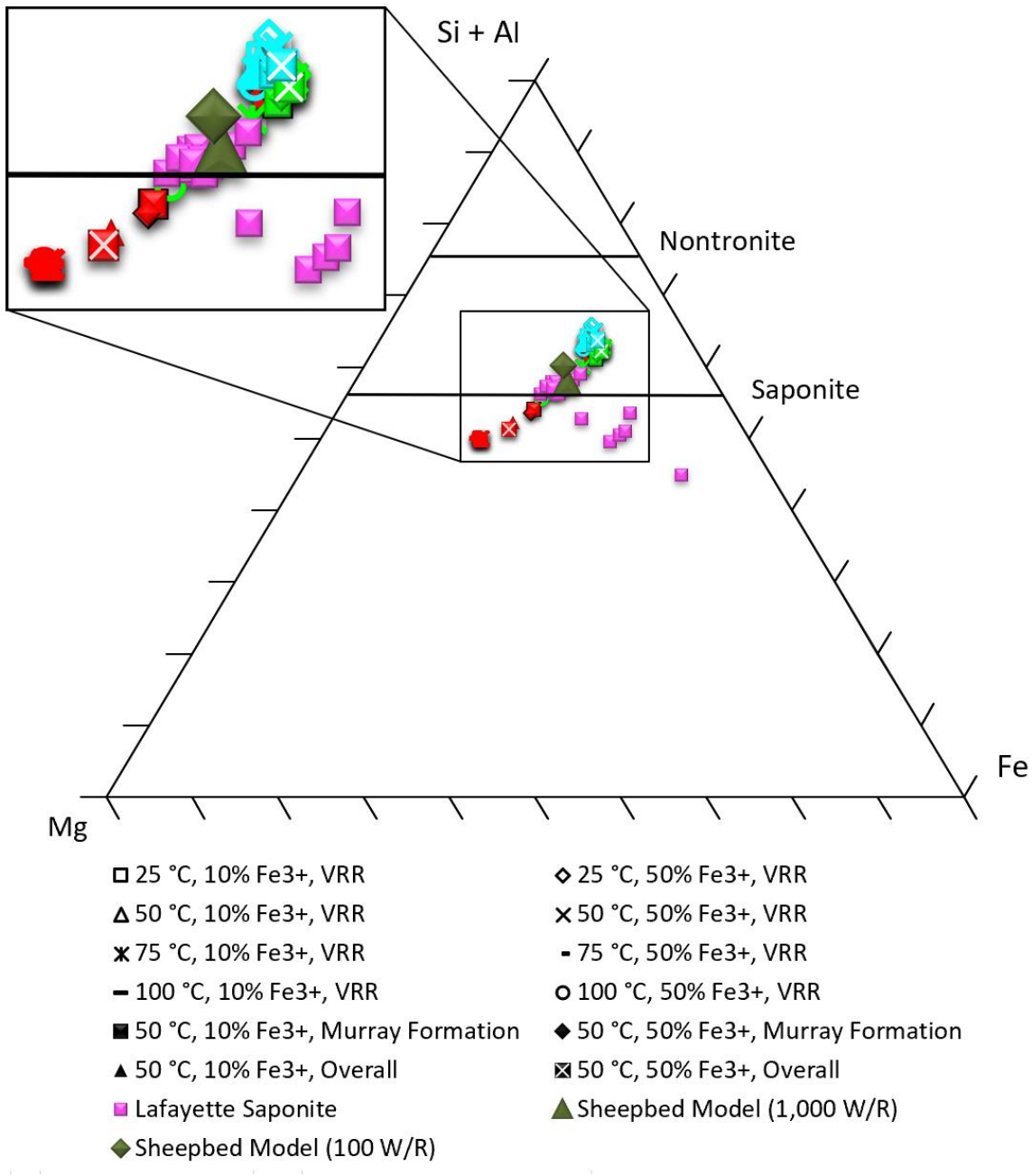

Figure 12: Mg-Si+Al-Fe_{tot} at. ternary plot. Results at 10,000 (red), 1,000 (green) and 100 (blue) W/R from the thermochemical models in this paper are plotted with some additional data from other sources for comparison. Lafayette saponite data taken from Hicks et al. (2014). CHIM-XPT results for the Sheepbed unit from Bridges et al. (2015b) at 100 W/R are shown for comparison.

SUPPLEMENTARY MATERIAL

Table S1. Table outlining the crystal chemistries for the magmatic phases in Oudam, Marimba, Quela, Sebina, Duluth, Stoer, Highfield and Rock Hall.

Sample	Plagioclase	Alkali feldspar	Orthopyroxene
Oudam	An40(7)[a]	-	$Mg_{0.79(7)}Fe_{1.20(8)}Ca_{0.01(4)}Si_2O_6$[c]
Marimba	An39(5)[a]	$K_{0.76(13)}Na_{0.24}Al_1Si_3O_8$[b]	$Mg_{0.79(7)}Fe_{1.20(8)}Ca_{0.01(4)}Si_2O_6$[c]
Quela	An39(6)[a]	$K_{0.65(18)}Na_{0.35}Al_1Si_3O_8$[b]	$Mg_{0.79(7)}Fe_{1.20(8)}Ca_{0.01(4)}Si_2O_6$[c]
Sebina	An42(6)[a]	$K_{0.65(18)}Na_{0.35}Al_1Si_3O_8$[b]	$Mg_{0.79(7)}Fe_{1.20(8)}Ca_{0.01(4)}Si_2O_6$[c]
Duluth	An34(4)[d]	$K_{0.65(18)}Na_{0.35}Al_1Si_3O_8$[b]	$Mg_{0.79(7)}Fe_{1.20(8)}Ca_{0.01(4)}Si_2O_6$[c]
Stoer	An41(4)[d]	$K_{0.65(18)}Na_{0.35}Al_1Si_3O_8$[b]	$Mg_{0.79(7)}Fe_{1.20(8)}Ca_{0.01(4)}Si_2O_6$[c]
Highfield	An28(3)[d]	$K_{0.65(18)}Na_{0.35}Al_1Si_3O_8$[b]	$Mg_{0.79(7)}Fe_{1.20(8)}Ca_{0.01(4)}Si_2O_6$[c]
Rock Hall	An44(7)[d]	$K_{0.65(18)}Na_{0.35}Al_1Si_3O_8$[b]	$Mg_{0.79(7)}Fe_{1.20(8)}Ca_{0.01(4)}Si_2O_6$[c]

[a] derived by Achilles et al. (2020). [b] values for average Murray formation for alkali feldspar derived by Morrison et al. (2018b). [c] values for average Yellowknife Bay for orthopyroxene derived by Morrison et al. (2018b). [d] derived by Rampe et al. (2020).

Table S2. Table detailing calculated alteration compositions for Oudam, Marimba, Quela, Sebina, Duluth, Stoer, Highfield and Rock Hall. Errors propagated from APXS accuracy, uncertainty in CheMin mineral abundances and uncertainties associated with magmatic phase crystal chemistry. Source data take from Achilles et al. (2020) and Rampe et al. (2020).

	Oudam	Marimba	Quela	Sebina
SiO_2	48.83 ± 2.55	47.33 ± 1.32	44.85 ± 1.47	45.38 ± 1.44
TiO_2	1.77 ± 0.07	1.37 ± 0.04	1.38 ± 0.05	1.30 ± 0.04
Al_2O_3	5.08 ± 0.49	6.18 ± 0.40	5.79 ± 0.49	6.45 ± 0.39
Cr_2O_3	0.54 ± 0.02	0.42 ± 0.01	0.38 ± 0.01	0.45 ± 0.02
FeO_T	29.30 ± 0.98	28.47 ± 0.61	23.79 ± 0.56	22.91 ± 0.70
MnO	0.37 ± 0.02	0.11 ± 0.01	0.29 ± 0.01	0.25 ± 0.01
MgO	7.42 ± 0.40	5.74 ± 0.25	4.99 ± 0.18	5.75 ± 0.31
CaO	0.40 ± 0.65	2.19 ± 0.38	5.47 ± 0.32	4.57 ± 0.30
Na_2O	1.56 ± 0.26	1.51 ± 0.12	1.51 ± 0.21	1.89 ± 0.20
K_2O	1.46 ± 0.08	0.71 ± 0.12	0.65 ± 0.10	0.71 ± 0.08
P_2O_5	0.88 ± 0.09	1.34 ± 0.09	1.45 ± 0.10	0.86 ± 0.07
SO_3	1.81 ± 0.31	4.02 ± 0.47	8.14 ± 0.27	8.12 ± 0.32
Cl	0.59 ± 0.02	0.61 ± 0.03	1.33 ± 0.03	1.35 ± 0.26

	Duluth	Stoer	Highfield	Rock Hall
SiO_2	38.34 ± 1.33	42.91 ± 2.24	53.84 ± 2.18	35.91 ± 3.25
TiO_2	1.49 ± 0.05	1.64 ± 0.06	1.31 ± 0.05	1.69 ± 0.09
Al_2O_3	3.49 ± 0.34	3.36 ± 0.64	6.66 ± 0.59	3.10 ± 1.09
Cr_2O_3	0.48 ± 0.04	0.46 ± 0.05	0.42 ± 0.05	0.52 ± 0.03
FeO_T	29.71 ± 0.86	29.46 ± 0.99	23.46 ± 1.07	28.19 ± 2.28
MnO	0.36 ± 0.04	0.27 ± 0.02	0.22 ± 0.02	0.13 ± 0.02
MgO	3.28 ± 0.31	6.17 ± 0.36	5.54 ± 0.44	4.65 ± 1.11
CaO	6.72 ± 0.37	3.32 ± 0.67	1.29 ± 0.54	3.67 ± 1.17
Na_2O	1.09 ± 0.20	1.25 ± 0.25	1.28 ± 0.24	1.40 ± 0.28
K_2O	0.93 ± 0.11	1.10 ± 0.27	1.01 ± 0.13	1.05 ± 0.06
P_2O_5	1.56 ± 0.10	1.31 ± 0.08	1.17 ± 0.08	1.47 ± 0.10
SO_3	11.25 ± 0.45	7.30 ± 0.85	2.44 ± 0.72	14.69 ± 1.55
Cl	1.30 ± 0.05	1.45 ± 0.06	1.37 ± 0.07	3.54 ± 0.16

Table S3. Table detailing rationale for minerals prevented from forming in CHIM-XPT (Reed et al., 2010) thermochemical modelling. For acmite, akermanite, antigorite, Fe-anthophyllite, ferro-actinolite, bredigite, grunerite, jennite, pyroxmangite, riebeckite, tobermorite, tremolite, wollastonite see Melwani Daswani et al. (2016).

Mineral	Rationale	Reference
Al-free_chlorite	Caused convergence issues during modeling.	

Belite	Industrial mineral in cement.	Tantawy et al., 2014
Clinozoisite	Clinozoisite-epidote series, members occur from ~130 bar and 320°C.	Deer et al., 2013 and references therein
Deerite	Forms from 200 °C and 8 kbar.	Vernié et al., 1986 and references therein
Diopside	Ca clinopyroxene. In series with hedenbergite.	Deer et al., 2013 and references therein
Epidote, Fe-epidote	Clinozoisite-epidote series, members occur from ~130 bar and 320°C.	Deer et al., 2013 and references therein
Hedenbergite	Ca clinopyroxene. In series with diopside.	Deer et al., 2013 and references therein
Larnite-bredigite	Solid solution of larnite and bredigite. Ca-silicate. Forms in contact metamorphism of carbonates.	Melwani Daswani et al., 2016 and references therein.
Prehnite	Forms at 200-300 °C.	Robinson & Bevans, 1999
Rankinite	High temperature Ca-silicate phase.	Treiman & Essene, 1983
Rhodonite	Pyroxenoid	Pinckney & Burnham, 1988
Tephroite	Mn-olivine	Deer et al., 2013 and references therein
Tilleyite	Occurs in contact metamorphic zone between igneous rocks and limestones. Low pressure, high-T.	Harker, 1959
tr.625ac.25prg.125	Solid solution of tremolite, actinolite and paragonite	Melwani Daswani et al., 2016 and references therein
Vesuvianite	Requires T > 360 °C and P> 50 bar.	Deer et al., 2013 and references therein

Table S4. Details of mean alteration compositions for the Murray formation, VRR, and an overall composition. Errors propagated from APXS accuracy errors, uncertainty in CheMin mineral abundances and uncertainties associated with magmatic phase crystal chemistry. Standard deviations for each mean is also detailed. Source data take from Achilles et al. (2020) and Rampe et al. (2020).

	Pre-VRR Murray*		VRR Murray		Overall*	
	Mean	Standard Deviation	Mean	Standard Deviation	Mean	Standard Deviation
SiO_2	46.60 ± 3.48	1.83	44.22 ± 4.79	9.04	45.58 ± 5.72	5.52
TiO_2	1.45 ± 0.10	0.21	1.55 ± 0.12	0.21	1.49 ± 0.16	0.20
Al_2O_3	5.87 ± 0.92	0.60	4.37 ± 1.70	1.99	5.23 ± 1.66	1.46
Cr_2O_3	0.45 ± 0.03	0.07	0.47 ± 0.07	0.05	0.46 ± 0.08	0.06
FeO_T	26.12 ± 1.45	3.23	27.04 ± 2.73	3.16	26.51 ± 3.08	2.97

MnO	0.25 ± 0.04	0.11	0.21 ± 0.04	0.07	0.24 ± 0.04	0.09
MgO	5.97 ± 0.56	1.03	5.45 ± 1.27	0.76	5.75 ± 1.38	0.89
CaO	3.16 ± 5.19	2.30	2.76 ± 2.12	1.29	2.99 ± 1.69	1.80
Na_2O	1.62 ± 0.41	0.18	1.31 ± 0.42	0.08	1.49 ± 0.60	0.21
K_2O	0.88 ± 0.23	0.39	1.05 ± 0.29	0.04	0.96 ± 0.36	0.29
P_2O_5	1.13 ± 0.18	0.30	1.32 ± 0.16	0.15	1.21 ± 0.23	0.25
SO_3	5.52 ± 1.19	3.14	8.14 ± 3.00	6.17	6.64 ± 2.03	4.43
Cl	0.97 ± 0.20	0.43	2.12 ± 0.15	1.23	1.46 ± 0.32	0.99

*Not including Duluth.

Table S5. Hematite wt.% at high (10,000), intermediate (1,000) and low (100) W/R ratios in thermochemical models (Figures 5 and 6) and using the calculated VRR mean alteration composition (Table S4) as the host rock (at both 10 and 50% Fe^{3+}/Fe_{tot}) reacted with GPW (Bridges et al., 2015b) at 50, 75 and 100 °C using CHIM-XPT (Reed et al., 2010).

	10% Fe^{3+}/Fe_{tot} Models			50% Fe^{3+}/Fe_{tot} Models		
	10,000 W/R	1,000 W/R	100 W/R	10,000 W/R	1,000 W/R	100 W/R
50 °C	28.6	2.1	0.0	29.3	1.9	3.6
75 °C	35.8	9.6	0.0	36.7	12.0	3.0
100 °C	36.4	14.5	0.0	37.9	19.2	9.0

Table S6. Pyrite wt.% at high (10,000), intermediate (1,000) and low (100) W/R ratios in thermochemical models (Figures 5 and 6) using the calculated VRR mean alteration composition (Table S4) as the host rock (at both 10 and 50% Fe^{3+}/Fe_{tot}) reacted with GPW (Bridges et al., 2015b) at 25, 50, 75 and 100 °C using CHIM-XPT (Reed et al., 2010).

	10% Fe^{3+}/Fe_{tot} Models			50% Fe^{3+}/Fe_{tot} Models		
	10,000 W/R	1,000 W/R	100 W/R	10,000 W/R	1,000 W/R	100 W/R
25 °C	10.8	9.9	9.0	9.2	8.4	8.1
50 °C	12.4	10.0	4.6	10.5	8.5	8.1
75 °C	15.4	10.0	9.0	13.0	8.5	8.1
100 °C	15.1	10.0	8.8	13.1	8.5	7.9

Table S7. Summed nontronite wt.% at high (10,000), intermediate (1,000) and low (100) W/R ratios in thermochemical models (Figures 5 and 6) using the calculated VRR mean alteration composition (Table S4) as the host rock (at both 10 and 50% Fe^{3+}/Fe_{tot}) reacted with GPW (Bridges et al., 2015b) at 25, 50, 75 and 100 °C using CHIM-XPT (Reed et al., 2010).

	10% Fe^{3+}/Fe_{tot} Models			50% Fe^{3+}/Fe_{tot} Models		
	10,000 W/R	1,000 W/R	100 W/R	10,000 W/R	1,000 W/R	100 W/R
25 °C	55.1	62.0	38.2	52.2	65.3	52.1
50 °C	0.0	60.1	33.5	0.0	63.3	54.5
75 °C	0.0	36.8	32.5	0.0	32.7	52.2
100 °C	0.0	23.4	30.2	0.0	12.2	34.3

Table S8. Summed clay wt.% at high (10,000), intermediate (1,000) and low (100) W/R ratios in models for the VRR mean composition (Table S4), at both 10 and 50% Fe^{3+}/Fe_{tot}, reacted with GPW (Bridges et al., 2015b) at 25, 50, 75 and 100 °C using CHIM-XPT (Reed et al., 2010).

	10% Fe^{3+}/Fe_{tot}			50% Fe^{3+}/Fe_{tot}		
	10,000 W/R	1,000 W/R	100 W/R	10,000 W/R	1,000 W/R	100 W/R
25 °C	77.8	84.5	64.9	74.3	86.5	71.9
50 °C	34.4	84.3	63.5	34.0	86.2	76.2
75 °C	42.9	65.8	62.6	42.4	60.8	78.2
100 °C	42.9	54.9	60.9	43.3	43.9	62.4

Table S9. Summed chlorite wt.% at high (10,000), intermediate (1,000) and low (100) W/R ratios in models for the VRR mean composition (Table S4), at both 10 and 50% Fe^{3+}/Fe_{tot}, reacted with GPW (Bridges et al., 2015b) at 25, 50, 75 and 100 °C using CHIM-XPT (Reed et al., 2010).

	10% Fe^{3+}/Fe_{tot}			50% Fe^{3+}/Fe_{tot}		
	10,000 W/R	1,000 W/R	100 W/R	10,000 W/R	1,000 W/R	100 W/R

25 °C	15.1	11.9	10.4	15.8	10.5	5.1
50 °C	34.4	12.9	11.5	34.0	11.5	6.7
75 °C	42.9	19.7	13.0	42.4	20.2	7.9
100 °C	42.9	23.8	15.0	43.3	15.0	14.7

Table S10. Summed talc wt.% at high (10,000), intermediate (1,000) and low (100) W/R ratios in models for the VRR mean composition (Table S4), at both 10 and 50% Fe^{3+}/Fe_{tot}, reacted with GPW (Bridges et al., 2015b) at 25, 50, 75 and 100 °C using CHIM-XPT (Reed et al., 2010).

	10% Fe^{3+}/Fe_{tot}			50% Fe^{3+}/Fe_{tot}		
	10,000 W/R	1,000 W/R	100 W/R	10,000 W/R	1,000 W/R	100 W/R
25 °C	7.4	10.5	19.8	6.3	10.6	14.7
50 °C	0.0	11.4	18.4	0.0	11.3	14.9
75 °C	0.0	9.3	17.1	0.0	7.9	15.2
100 °C	0.0	7.7	15.8	0.0	5.4	13.5

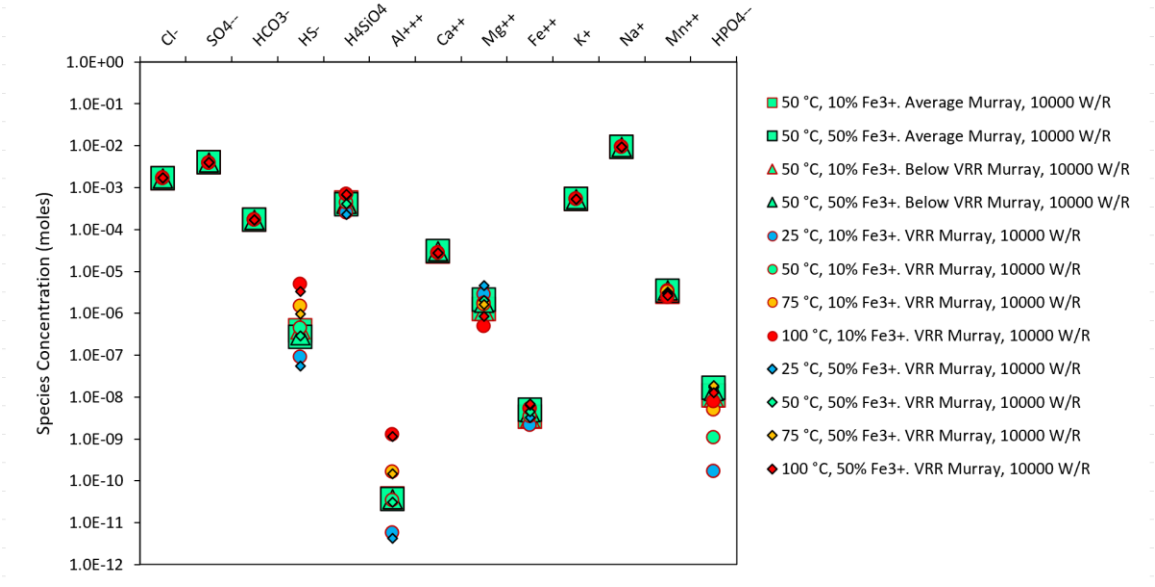

Figure S1. Modeled fluid composition at high (10000) W/R for all three alteration derived alteration compositions (Table S4) for all modeled temperatures and Fe^{3+}/Fe_{tot}.

Supporting Information References

Achilles C.N., Rampe E.B., Downs R.T., Bristow T.F., Ming D.W., Morris R.V., Vaniman D.T., Blake D.F., Yen A.S., McAdam A.C., Sutter B., Fedo C.M., Gwizd S., Thompson L.M., Gellert R., Morrison S.M., Treiman A.H., Crisp J.A., Gabriel T.S.J., Chipera S.J., Hazen R.M., Craig P.I., Thorpe M.T., Des Marais D.J., Grotzinger J.P., Tu V.M., Castle N.,

Downs G.W., Peretyazhko T.S., Walroth R.C., Sarrazin P., and Morookian J.M. 2020. Mineralogy of ancient fluvial-lacustrine sediments in Gale crater, Mars: Evidence for multiple diagenetic episodes. Journal of Geophysical Research: Planets, 125, e2019JE006295.

Bridges J.C., Schwenzer S.P., Leveille R., Westall F., Wiens R.C., Mangold N., Bristow T., Edwards P., and Berger G. 2015b. Diagenesis and Clay mineral Formation in Gale Crater, Mars. J. Geophys. Res. Planets, 120, 1-19, doi:10.1002/2014JE004757.

Deer W.A., Howie R.A., and Zussman J. 2013. An introduction to the rock-forming minerals. 3rd edition. The Mineralogical Society, London.

Harker R.I. 1959. The synthesis and stability of tilleyite, Ca5Si2O7(CO3)2. American Journal of Science, 257(9), 656-667.

Melwani Daswani M., Schwenzer S.P., Reed M.H., Wright I.P., and Grady M.M. 2016. Alteration minerals, fluids, and gases on early Mars: Predictions from 1-D flow geochemical modeling of mineral assemblages in meteorite ALH 84001. Meteoritics & Planetary Science, 51(11), 2154-2174.

Morrison S.M., Downs R.T., Blake D.F., Vaniman D.T., Ming D.W., Hazen R.M., Treiman A.H., Achilles C.N., Yen A.S., Morris R.V., Rampe E.B., Bristow T.F., Chipera S.J., Sarrazin P.C., Gellert R., Fendrich K.V., Morookian J.M., Farmer J.D., Des Marais D.J., and Craig P.I. 2018. Crystal chemistry of martian minerals from Bradbury Landing through Naukluft Plateau, Gale crater, Mars. Am. Mineral. 103(6), 857-871.

Pinckney L.R. and Burnham C.W. 1988. Effects of compositional variation on the crystal structures of pyroxmangite and rhodonite. American Mineralogist, 73(7-8), 798-808.

Rampe E.B., Bristow T.F., Morris R.V., Morrison S.M., Achilles C.N., Ming D.W., Vaniman D.T., Blake D.F., Tu V.M., Chipera S.J., Yen A.S., Peretyazhko T.S., Downs R.T., Hazen R.M., Treiman A.H., Grotzinger J.P., Castle N., Craig P.I., Des Marais D.J., Thorpe M.T., Walroth R.C., Downs G.W., Fraeman A.A., Siebach K.L., Gellert R., Lafuente B., McAdam A.C., Meslin P.-Y., Sutter B., and Salvatore M.R. 2020b. Mineralogy of Vera Rubin ridge from the Mars Science Laboratory CheMin instrument. Journal of Geophysical Research: Planets, 125, e2019E006306.

Reed M.H., Spycher N.F., and Palandri J. 2010. User Guide for CHIM-XPT: A Program for Computing Reaction Processes in Aqueous-Mineral-Gas Systems and MINTAB Guide. 71p., University of Oregon, Eugene.

Robinson D. and Bevins R.E. 1999. Patterns of regional low-grade metamorphism in metabasites, in Low-Grade Metamorphism, edited by M. Frey and D. Robinson, pp. 143–168, Blackwell Sci, Oxford, U.K.

Tantawy M.A., Shatat M.R., El-Roudi A.M., Taher M.A., and Abd-El-Hamed M. 2014. Low temperature synthesis of belite cement based on silica fume and lime. International scholarly research notices, 2014.

Treiman A.H. and Essene E.J. 1983. Phase equilibria in the system CaO-SiO2-CO2. American Journal of Science A, 283, 97-120.

Vernié P., Kienast J.R. and Mével C. 1986. The occurrence of deerite in highly oxidizing conditions within the ‘schistes lustrés’ of eastern Corsica. Journal of Metamorphic Geology, 4(4), 385-399.